Clim Dyn
DOI 10.1007/s00382-010-0954-4

An assessment of oceanic variability in the NCEP climate forecast system reanalysis

Yan Xue · Boyin Huang · Zeng-Zhen Hu · Arun Kumar · Caihong Wen · David Behringer · Sudhir Nadiga

Received: 10 June 2010 / Accepted: 23 November 2010

Abstract At the National Centers for Environmental Prediction (NCEP), a reanalysis of the atmosphere, ocean, sea ice and land over the period 1979–2009, referred to as the climate forecast system reanalysis (CFSR), was recently completed. The oceanic component of CFSR includes many advances: (a) the MOM4 ocean model with an interactive sea-ice, (b) the 6 h coupled model forecast as the first guess, (c) inclusion of the mean climatological river runoff, and (d) high spatial (0.5° × 0.5°) and temporal (hourly) model outputs. Since the CFSR will be used by many in initializing/validating ocean models and climate research, the primary motivation of the paper is to inform the user community about the saline features in the CFSR ocean component, and how the ocean reanalysis compares with in situ observations and previous reanalysis. The net ocean surface heat flux of the CFSR has smaller biases compared to the sum of the latent and sensible heat fluxes from the objectively analyzed air-sea fluxes (OAFlux) and the shortwave and longwave radiation fluxes from the International Satellite Cloud Climatology Project (ISCCP-FD) than the NCEP/NCAR reanalysis (R1) and NCEP/DOE reanalysis (R2) in both the tropics and extratropics. The ocean surface wind stress of the CFSR has smaller biases and higher correlation with the ERA40 produced by the European Centre for Medium-Range Weather Forecasts than the R1 and R2, particularly in the tropical Indian and Pacific Ocean. The CFSR also has smaller errors compared to the QuickSCAT climatology for September 1999 to October 2009 than the R1 and R2. However, the trade winds of the CFSR in the central equatorial Pacific are too strong prior to 1999, and become close to observations once the ATOVS radiance data are assimilated in late 1998. A sudden reduction of easterly wind bias is related to the sudden onset of a warm bias in the eastern equatorial Pacific temperature around 1998/1999. The sea surface height and top 300 m heat content (HC300) of the CFSR compare with observations better than the GODAS in the tropical Indian Ocean and extratropics, but much worse in the tropical Atlantic, probably due to discontinuity in the deep ocean temperature and salinity caused by the six data streams of the CFSR. In terms of climate variability, the CFSR provides a good simulation of tropical instability waves and oceanic Kelvin waves in the tropical Pacific, and the dominant modes of HC300 that are associated with El Nino and Southern Oscillation, Indian Ocean Dipole, Pacific Decadal Oscillation and Atlantic Meridional Overturning Circulation.

Y. Xue (✉) · B. Huang · Z.-Z. Hu · A. Kumar · C. Wen
Climate Prediction Center, NCEP/NOAA, 5200 Auth Road, Room 605, Camp Springs, MD 20746, USA
e-mail: Yan.Xue@noaa.gov

B. Huang · C. Wen
Wyle Information System, Camp Springs, MD, USA

D. Behringer · S. Nadiga
Environmental Modeling Center, NCEP/NOAA, Camp Springs, MD, USA

1 Introduction

Ocean initialization plays a critical role in seasonal-to-decadal climate predictions since most of predictability on those time scales comes from the ocean memory (Guilyardi et al. 2009; Meehl et al. 2009). The National Centers for Environmental Prediction (NCEP) has been involved in the development of an ocean data assimilation system (ODAS) for initialization of its operational coupled ocean–atmosphere forecast systems since the early 1990s. The first

Published online: 09 December 2010

version of the NCEP's ODAS was based on the Geophysical Fluid Dynamics Laboratory (GFDL) Modular Ocean Model (MOM) version 1 (MOM1) and configured for the Pacific Ocean (Ji et al. 1995). A global ocean data assimilation system (GODAS) was implemented in 2004 (Behringer and Xue 2004). Since then, many experimental GODAS simulations have been conducted to assess the impacts of assimilating Argo salinity profiles (Huang et al. 2008), of increasing the depth of the assimilation and of modifying the assimilation method to be multivariate in velocity (Behringer 2007).

The current operational GODAS is based on the GFDL MOM version 3 in a quasi-global (65°S–65°N) configuration with 40 vertical levels and a horizontal resolution of 1° × 1° with an equatorial meridional resolution of 1/3° resolution within 10° of the equator. The GODAS is updated daily with a 2-day delay, and pentad and monthly averages are used for real-time global ocean monitoring products (http://www.cpc.ncep.noaa.gov/products/GODAS).

A common practice for initialization of the ocean component of a coupled forecast system is to assimilate various ocean observations into an ocean model forced by atmospheric fluxes. For operational ocean analysis, a hierarchy of ocean data assimilation methods have been adopted at different centers, which range from optimal interpolation (OI) (Balmaseda et al. 2008), three-dimensional variational (3D-VAR) (Behringer et al. 1998), and Kalman filter (Keppenne et al. 2008). In all these methods, the analysis of the oceanic and atmospheric component is done separately. A potential drawback of a separate oceanic and atmospheric assimilation is that imbalances between atmospheric and oceanic initial conditions often result in initialization shocks and degrade the model's forecast skill (Schneider et al. 1999). As a step forward, several groups have been developing coupled ocean and atmosphere data assimilation systems (Zhang et al. 2007).

Recently, at the NCEP, a new partially coupled ocean and atmosphere data assimilation system was developed and was used for the reanalysis of the atmosphere, ocean, sea ice and land for 1979–2009 (CFSR, Saha et al. 2010). The primary motivation for the CFSR was to provide ocean, atmosphere, and land initial conditions for a reforecast of the climate forecast system (CFS) version 2, CFSv2, for skill estimation and for the calibration of real-time forecasts. The CFSR will also be extended as an operational, real-time analysis system. Compared to the NCEP/NCAR Reanalysis (referred to as R1, Kalnay et al. 1996) and the NCEP/DOE Reanalysis (referred to as R2, Kanamitsu et al. 2002), some of the major advances in the CFSR include (1) a 6-h coupled forecast for the first guess field, (2) an interactive sea-ice model, (3) assimilation of satellite radiances, (4) a high resolution atmospheric and oceanic model, and (5) observed variations in CO_2, aerosols and other trace gases and solar variations etc. For details about the CFSR, see Saha et al. (2010).

Although the primary motivation of the CFSR was to provide the best analysis of different components of the Earth system from the perspective of forecast initialization and improved prediction skill, the availability of a reanalysis from 1979 to present is an opportunity to also use it in the context of climate research and climate monitoring. With that goal, we provide a comprehensive evaluation of the oceanic variability in the CFSR. We first quantify the mean biases, linear correlations and root-mean-square differences between the CFSR and observations, as well as with previous analyses, in both the ocean surface fluxes and oceanic fields. We also assess the capability of the CFSR in simulating tropical instability waves and oceanic Kelvin waves in the tropical Pacific, and documenting the dominant modes of upper ocean heat content variability associated with El Nino and Southern Oscillation (ENSO), Indian Ocean Dipole (IOD), Pacific Decadal Oscillation (PDO), and Atlantic Meridional Overturning Circulation (AMOC). Other aspects of the CFSR are examined in accompanying papers, including an assessment of the surface climate variability (Wang et al. 2010), troposphere (Chelliah et al. 2010), and stratosphere (Long et al. 2010) variability.

The paper is organized into six sections. Section 2 provides a description of the GFDL MOM4 ocean model, the 3DVAR analysis scheme, and ocean observations used in the assimilation. Section 3 describes various data sets that are used for the validation. Section 4 discusses the results of the validation for the climatology and variability in the CFSR. In Sect. 5, we assess and describe the dominant modes of climate variability in the CFSR. The summary and conclusions are given in Sect. 6.

2 The oceanic component of the CFSR

2.1 The ocean model

For its ocean component, the CFSR uses the GFDL MOM version 4p0d (MOM4) (Griffies et al. 2004). The zonal resolution of the MOM4 is 1/2°. The meridional resolution is 1/4° between 10°S and 10°N, gradually increasing through the tropics to 1/2° poleward of 30°S and 30°N. There are 40 layers in the vertical with 27 layers in the upper 400 m of the ocean, and the maximum depth is approximately 4.5 km. The vertical resolution is 10 m from the surface to 240 m depth, gradually increasing to about 511 m in the bottom layer. Compared to the MOM3 used in the current GODAS, the MOM4 is fully global with an interactive sea-ice model, while the MOM3 is truncated at 64°N and 74°S. In addition, the new configuration

includes a mean climatological river runoff specified at the model coastline (Griffies et al. 2004).

2.2 The ocean data assimilation scheme

A 3-D variational (3DVAR) analysis scheme, adapted from Derber and Rosati (1989), has been modified to incorporate a temporal and spatial varying background error covariance (Behringer et al. 1998). The 3DVAR scheme minimizes a cost function that measures the distances between analysis and forecast weighted by the background error covariance, and the misfits between analysis and observations weighted by the observational error covariance. In the CFSR, the background error covariance matrix is univariate in temperature and salinity. The horizontal covariance is modeled using a diffusion equation, which approximates a Gaussian function that is stretched in the zonal direction with the stretching being greatest near the equator (Derber and Rosati 1989). The vertical covariance is similarly modeled by a diffusion equation with length scales specified as a function of depth such that at any level the scale is twice the level thickness. The variance is set proportional to the square-root of the local vertical temperature gradient computed from the forecast (Behringer et al. 1998). The observational errors are assumed to be uncorrelated. The errors assigned to a temperature profile vary with depth according to the square root of the vertical temperature gradient and are scaled to have values between 1°C and 2.5°C. The standard error assigned to a salinity profile is a constant 0.1 psu at all depths. Only the temperature data in the top 750 m are assimilated into the CFSR.

The assimilation cycle is completed at 00Z, 06Z, 12Z, and 18Z using the 6-h coupled model forecast as the first guess field (Saha et al. 2010). All observations from the previous 10-days are assimilated. The innovations are weighted, the most weight is given to model-observation differences closest to the time of the assimilation cycle. Such an assimilation window will inevitably introduce some lags, but we need to launch the forecasts as close as possible to the current real time for improvement of hindcast skill on lead times from weeks to seasons, and to do so we tolerate an asymmetrical observation window.

For the top level of the model (5 m), the temperature analysis is strongly nudged to the daily OI SST analysis (described in Sect. 2.3), and the salinity to the mean climatology based on the World Ocean Database 1998 (referred to as WOD1998) (Conkright et al. 1999). The relaxation is done at 6-h intervals. A relaxation coefficient of zero would mean no relaxation is done, while a coefficient of one would mean that the forecast field is replaced by the prescribed field. In the CFSR, the relaxation coefficient for both SST and SSS is set to 0.5. The purpose of using relaxation at the surface is to provide a strong constraint on the ocean at the interface with the atmosphere, and compensate for possible model drift due to errors in the surface heat and momentum fluxes.

It is important to point out that the CFSR is not a continuous dataset throughout the whole period of 1979–2009; rather it is a combination of six data streams, each from a different initial condition (Saha et al. 2010). The ocean initial condition to begin each data stream came from a stand-alone GODAS run that assimilates the same data sets, but is forced by surface fluxes from the R2. Doing the reanalysis in segments led to serious discontinuity in the deep ocean (Fig. 15), which will have consequences for decadal prediction. Cautions should be taken when the CFSR is used to study oceanic variability on decadal time scales.

2.3 The ocean observations

The temperature observations used in the assimilation include profiles from expendable bathythermographs (XBTs), fixed mooring arrays—the Tropical Atmosphere Ocean/Triangle Trans Ocean Buoy Network (TAO/TRITON) (McPhaden et al. 1998) in the Pacific Ocean, the Prediction and Research Moored Array in the Tropical Atlantic (PIRATA) (Bourlès et al. 2008), the Research Moored Array for African–Asian–Australian Monsoon Analysis and Prediction (RAMA) in the tropical Indian Ocean (McPhaden et al. 2009), and from the Argo profiling floats (The Argo Science Team 2001). The XBT observations collected prior to 1990 are from the WOD1998 (Conkright et al. 1999), while XBTs collected subsequent to 1990 are from the Global Temperature-Salinity Profile Project (GTSPP) at http://www.nodc.noaa.gov/GTSPP.

Since subsurface salinity observations were extremely sparse prior to the advent of the Argo array, synthetic salinity profiles are assimilated in the CFSR. Each synthetic profile is constructed from an observed temperature profile and the local climatological T-S correlation based on the WOD1998 (Conkright et al. 1999). An important advantage of this approach is that it maintains water mass properties over the course of the analysis. The disadvantage is that some salinity variability is lost.

The altimetry sea surface height (SSH) data were not assimilated in the CFSR. The method that we used in assimilating altimetry in the GODAS (Behringer 2007) assimilates only the variable part of the altimetry data. To do this we require both a mean climatology of the observations and a mean climatology of the model. The model climatology requires a long run of the CFSR assimilating the same in situ data. This would require considerably greater computing resources (i.e., running the CFSR for climatology, and then running it again with the altimetry). So the altimetry will be included in the CFSR at a later stage.

As indicated above, temperature and salinity in the top level of the model are nudged to analyzed fields of observed sea surface temperature (SST) and sea surface salinity (SSS). The analyzed SST is the daily OI SST (Reynolds et al. 2007), which includes the AVHRR-only product version 1 from November 1981 through May 2002 and the AMSR+AVHRR product version 2 from June 2002 onward. From January 1979 through October 1981, the HadISST (Rayner et al. 2003) is used as the OI SST is not available prior to November 1981. The analyzed SSS is the annual mean climatology based on the WOD1998 (Conkright et al. 1999).

3 Validation data sets

We use various in situ observational and analyses data sets for validation of the CFSR. The latent heat flux (LHF) and sensible heat flux (SHF) are from the objectively analyzed air-sea fluxes (OAFlux) (Yu and Weller 2007) and the shortwave (SW) and longwave (LW) radiation heat fluxes are from the International Satellite Cloud Climatology Project (ISCCP-FD, Zhang et al. 2004). The LHF and SHF from the OAFlux have been validated against the heat flux estimates from the buoy observations, and its accuracy, evaluated at 105 buoys, is about 9.6 Wm^{-2} for LHF and 2.6 Wm^{-2} for SHF (Yu and Weller 2007). Uncertainties in the SW from the ISCCP-FD are estimated to be 5% (Large and Yeager 2009). The combination of the LHF and SHF from the OAFlux and the SW and LW from the ISCCP-FD (referred to as OA_ISCCP) provides an estimate for the net ocean surface heat flux (NFLX). The monthly LHF and SHF of the OAFlux from 1979–2009, and the monthly SW and LW of the ISCCP-FD from 1984–2007, were downloaded from http://oaflux.whoi.edu/index.html, and linearly interpolated to match the CSFR grid. Validation data sets for wind stress are often limited in space and time (Smith et al. 2001), and contain large uncertainties (Wittenberg 2004). We focus on an inter-comparison among four reanalysis wind stress products, namely R1, R2, CFSR and ERA40 (Uppala et al. 2005), for the common period 1979–2001 when the ERA40 is available. For the period when the QuickSCAT winds are available, a decade-long (September 1999–October 2009) Scatterometer Climatology of Ocean Winds (SCOW, http://numbat.coas.oregonstate.edu/scow/) is used for validation of the climatology for R1, R2 and CFSR during that period.

The monthly climatological temperature and salinity analysis from the World Ocean Atlas 2005 (WOA05) (Locarnini et al. 2006; Antonov et al. 2006) is used to validate the climatology of SSS and mixed layer depth (MLD) in the CFSR. For validation of seasonal temperature and upper ocean heat content, the objective seasonal temperature analysis from the National Oceanographic Data Center (NODC) (Levitus et al. 2009) is used. The NODC temperature analysis is at 16 levels ranging from the ocean surface to 700 m in depth on a global $1° \times 1°$ grid from 1955 to 2009. The temperature data was linearly interpolated to match the CFSR grid, and the upper ocean heat content is calculated as the average temperature in the upper 300 m (referred to as HC300). For validation of the CFSR salinity, the objective pentadal (5-year-running-mean) salinity analysis from the NODC is also used.

Since the altimetry SSH data (referred to as Altimetry hereafter) were not assimilated in the CFSR, it serves as an independent data set for validation. The daily Altimetry from 1993 to 2009 was downloaded from http://www.aviso.oceanobs.com, then averaged into monthly means and linearly interpolated to match the CFSR grid. For the validation of ocean surface currents, the pentad currents from Ocean Surface Current Analysis-Real Time (OSCAR) (Bonjean and Lagerloef 2002) were downloaded from http://www.oscar.noaa.gov. In addition, the monthly ocean temperature, ocean currents and surface wind measurements at four equatorial TAO moorings, and the objective equatorial TAO temperature analysis (Mike McPhaden, personal communication) were used in the validation.

4 Validation of the oceanic component of the CFSR

4.1 Ocean surface heat fluxes and wind stress

Air-sea fluxes of momentum, heat and moisture are the key to understanding atmospheric and oceanic variability and their interactions. Taylor (2000) review the state-of-the-art of air-sea flux estimation from various methods including reanalysis products. Despite significant deficiencies in the reanalysis products (Trenberth et al. 2001; Wang and McPhaden 1999; Smith et al. 2001; Stammer et al. 2004; Large and Yeager 2009), reanalysis fluxes are often used as forcing in ocean data assimilation systems (Balmaseda et al. 2008; Behringer and Xue 2004). The quality of the ocean analysis is often highly dependent on the quality of the reanalysis fluxes (Balmaseda and Anderson 2009). In this section, we provide an assessment of the reanalysis heat fluxes and wind stress simulated by the R1, R2, CFSR and ERA40. A complementary assessment of the fresh water fluxes is made by Wang et al. (2010).

4.1.1 Ocean surface heat fluxes

The net surface heat flux (NFLX) climatology of the R1, R2 and CFSR is compared with that of the OA_ISCCP (Fig. 1). The comparison results should be taken with

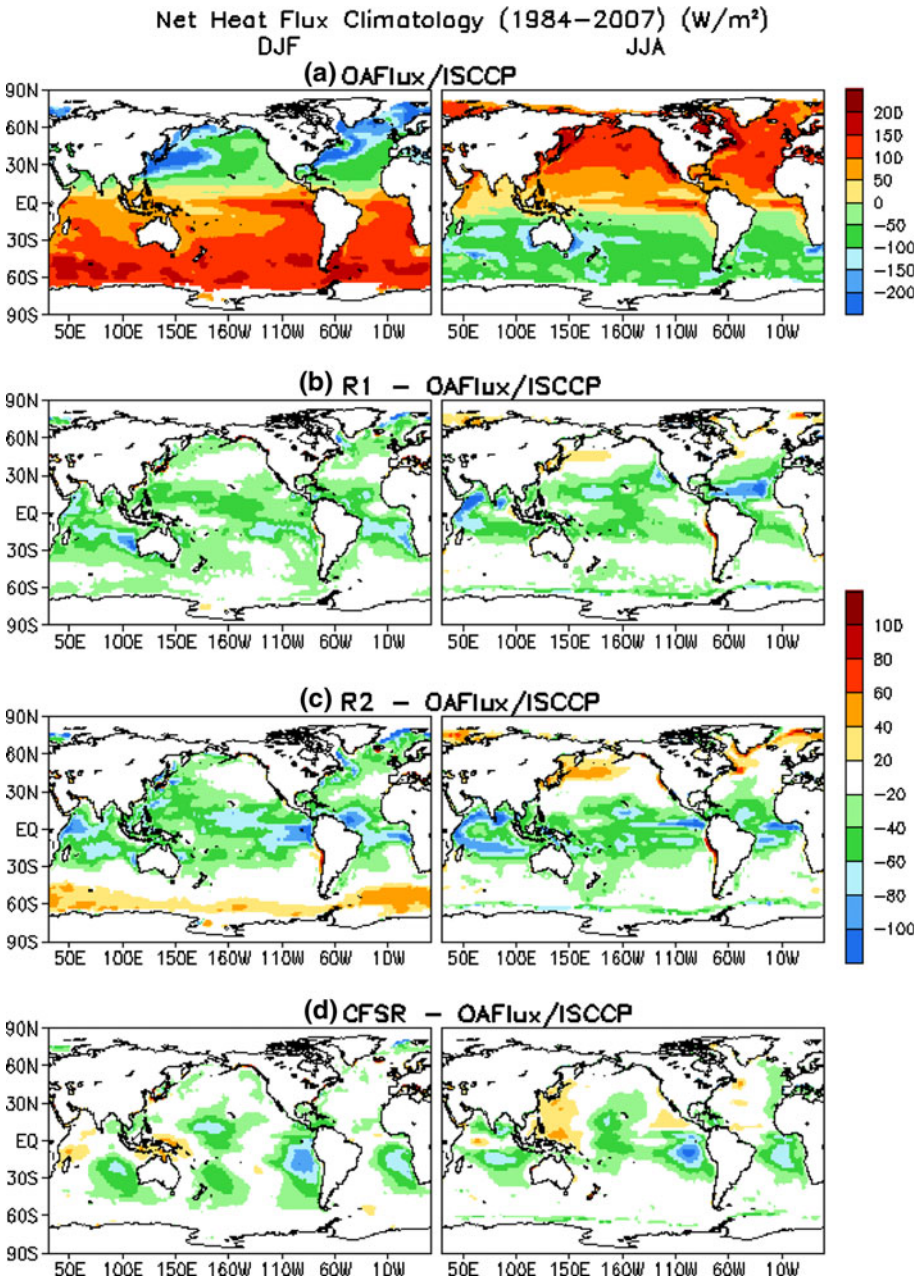

Fig. 1 The net ocean surface heat flux for Dec–Jan–Feb (*left column*) and for Jun–Jul–Aug (*right column*) averaged over 1984–2007. **a** OAFlux/ISCCP, **b** R1 minus OAFlux/ISCCP, **c** R2 minus OAFlux/ISCCP, **d** CFSR minus OAFlux/ISCCP. Unit is W/m^2

caution, since the SW in the ISCCP is overestimated by 5% (Large and Yeager 2009) and the OA_ISCCP has an imbalance of 30 W/m^2 over the global ocean. During boreal winter (DJF, left panel), the northern oceans lose heat with the largest values over 150 W/m^2 over the western boundary currents (Kuroshio Extension and Gulf Stream), while the tropical and southern oceans gain heat with maxima over 150 W/m^2 in the eastern equatorial Pacific and high-latitude southern oceans (Fig. 1a). During boreal summer (JJA, right panel), the tropical and northern oceans gain heat, while the southern oceans lose heat (Fig. 1a). In the subsequent discussion heat gain (loss) is referred to as ocean warming (cooling).

Compared to the OA_ISCCP, the R1 and R2 underestimate the warming in the tropics throughout the year, and overestimate the cooling over the western boundary currents during boreal winter (Fig. 1b, c). The cooling bias in boreal winter over the Kuroshio Extension and Gulf Stream is mostly eliminated in the CFSR, and the deficient heat gain in the tropics is also significantly reduced, except large negative biases exist in the southeastern tropical oceans (Fig. 1d). For most coupled GCMs, large warm biases exist in the southeastern Pacific and Atlantic, which have been attributed to a lack of low clouds and an overestimation of SW (Hu et al. 2008). Wang et al. (2010) compared the mean SW from the CFSR with the ensemble

mean SW from three observational analyses. They suggest that the SW in the CFSR is about 10–20 W/m^2 too weak in the southeastern tropical oceans, consistent with the negative biases in NFLX in those regions (Fig. 1d), but it is about 10–20 W/m^2 too strong in the tropical Indian Ocean, the western tropical Pacific, and the tropical North Atlantic due to deficiency in cloudiness.

A comparison of the year-to-year variability of NFLX, SW, LH, LW and SH is shown in Fig. 2. Although NFLX should be close to zero averaged in the global ocean over a long period, the NFLX averaged over the ocean between 60°S and 60°N for 1984–2007 in R1, R2, CFSR and OA_ISCCP is 4.5 W/m^2, 4.7, 14.7 and 30 W/m^2, respectively. In this sense, the budget closure in the CFSR may be worse than that in the R1 and R2. However, the imbalance in OA_ISCCP is as large as 30 W/m^2, which has been attributed to too strong amplitude of SW in ISCCP (Large and Yeager 2009). Imbalance in NFLX is also common in ocean heat flux products based on ship data (Berry and Kent 2009).

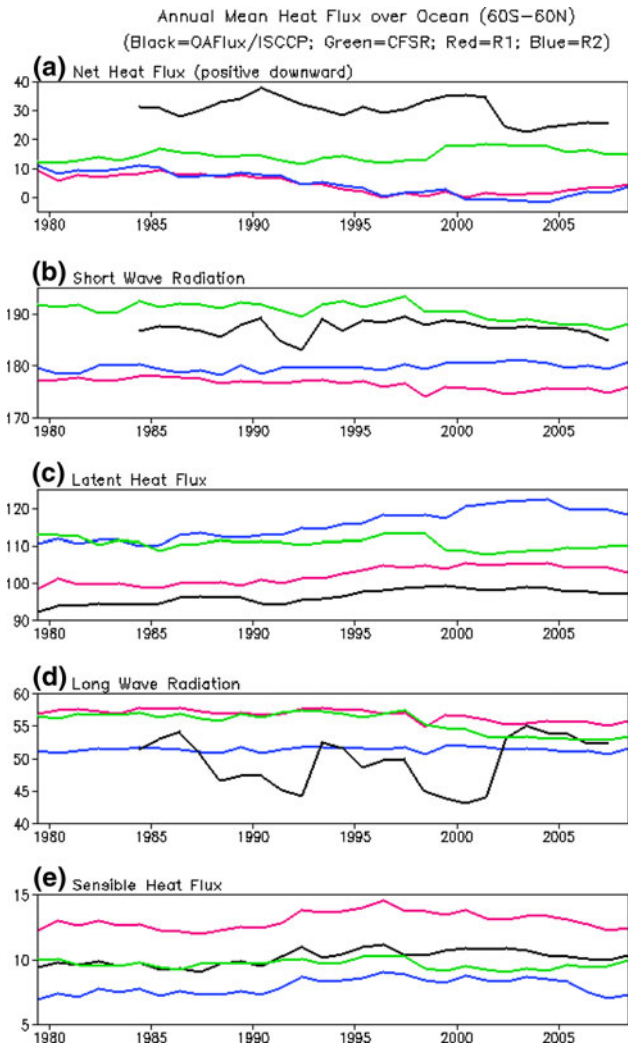

Fig. 2 Time series of the annual mean of the **a** net ocean surface heat flux, **b** short wave radiation, **c** latent heat flux, **d** long wave radiation, and **e** sensible heat flux averaged over the global ocean between 60°S and 60°N for the period 1979–2008 for OAFlux/ISCCP (*black line*), R1 (*red line*), R2 (*blue line*) and CFSR (*green line*). Unit is W/m^2

The global ocean mean NFLX from the R1 and R2 is at about 9 W/m^2 during the 1980s and it decreases steadily in the 1990s, remaining near zero during the 2000s (Fig. 2a). This indicates the global net heat flux imbalance is reduced as more observations become available. The global ocean mean NFLX from the CFSR stays at about 13 W/m^2 from 1979 to 1998, but it increases suddenly around 1998/1999 (Fig. 2a), which coincides with a sudden decrease of LH (Fig. 2c). Similar jumps are found in precipitation, humidity and other atmospheric variables and may be attributable to the assimilation of the ATOVS radiance data starting in October 1998 (Saha et al. 2010; Wang et al. 2010).

The SW from the CFSR is about 10–15 W/m^2 higher than that from the R1 and R2, and is close to that from the ISCCP-FD (Fig. 2b). The sharp decrease in SW from 1991 to 1993 is likely due to solar dimming caused by the injection of volcanic aerosol from the Mt. Pinatubo eruption in June 1991, which is missing in R1 and R2. The LH from the CFSR is about 10–15 W/m^2 larger than that of the R1 and OAFlux, and is very close to that of the R2 prior to 1998, but they depart abruptly from each other starting in 1999 (Fig. 2c). The LW of the CFSR is close to that of the R1, but it is about 5 W/m^2 larger than that of the R2 and ISCCP-FD. The low-frequency variation of LW is extremely large in the ISCCP-FD in contrast to the R1, R2, and CFSR. The ISCCP web site at http://isccp.giss.nasa.gov/projects/flux.html suggests that the large variation around 2002/2003 is associated with a spurious change of the atmospheric temperatures in the NOAA operational TOVS products that are used in the ISCCP calculation. However, all of the LWs converge after 2002. The uncertainties in SH are about 5 W/m^2 (Fig. 2e).

4.1.2 Ocean surface wind stress

Uncertainties in the reanalysis wind stress products are difficult to quantify due to a lack of validation data sets. Efforts have been made to estimate uncertainties of wind stress in the tropical Pacific (Wittenberg 2004; Trenberth et al. 2001), in the annual climatology (Josey et al. 2002), and in interannual variability (Smith et al. 2001). Different approaches have been used to correct reanalysis wind stress biases (Stammer et al. 2004; Large and Yeager 2009). Because of large uncertainties in observational estimates, here we intend to present an intercomparison among four reanalysis wind stress products, namely the R1, R2, CFSR and ERA40. The purpose is to illustrate the differences and similarities among the reanalysis products.

Compared to the ERA40, the R1 zonal (TAUX) and meridional (TAUY) wind stress are too weak in the

equatorial Pacific (Fig. 3a), which is consistent with the analyses by Wittenberg (2004), Stammer et al. (2004) and Large and Yeager (2009). For the R2, major differences from the ERA40 are stronger westerly wind stress in the mid-latitude North Pacific and North Atlantic during boreal winter and stronger westerly wind stress in the high-latitude southern oceans during boreal summer (Fig. 3b). The CFSR wind stress agrees well with the ERA40 wind stress except that it overestimates the strength of the trade winds in the central tropical Pacific, and the westerly wind in the high-latitude southern oceans during boreal summer (Fig. 3c). For anomaly correlation, it is relatively low (less than 0.7) in the tropics, but very high (greater than 0.9) in the extra-tropics. The CFSR generally agrees with the ERA40 better than the R1 and R2 in the tropical Indian and Pacific. For both TAUX and TAUY, the correlation in the tropical Atlantic is much lower than that in the tropical Indian and Pacific Oceans, indicating poor agreements among the reanalysis products in the tropical Atlantic.

The climatology differences from the ERA40 (Fig. 3) can be compared with the climatology differences from the QuickSCAT SOCW (Risien and Chelton 2008) for the period from September 1999 to October 2009 (Fig. 4). Risien and Chelton (2008) conducted a detail comparison

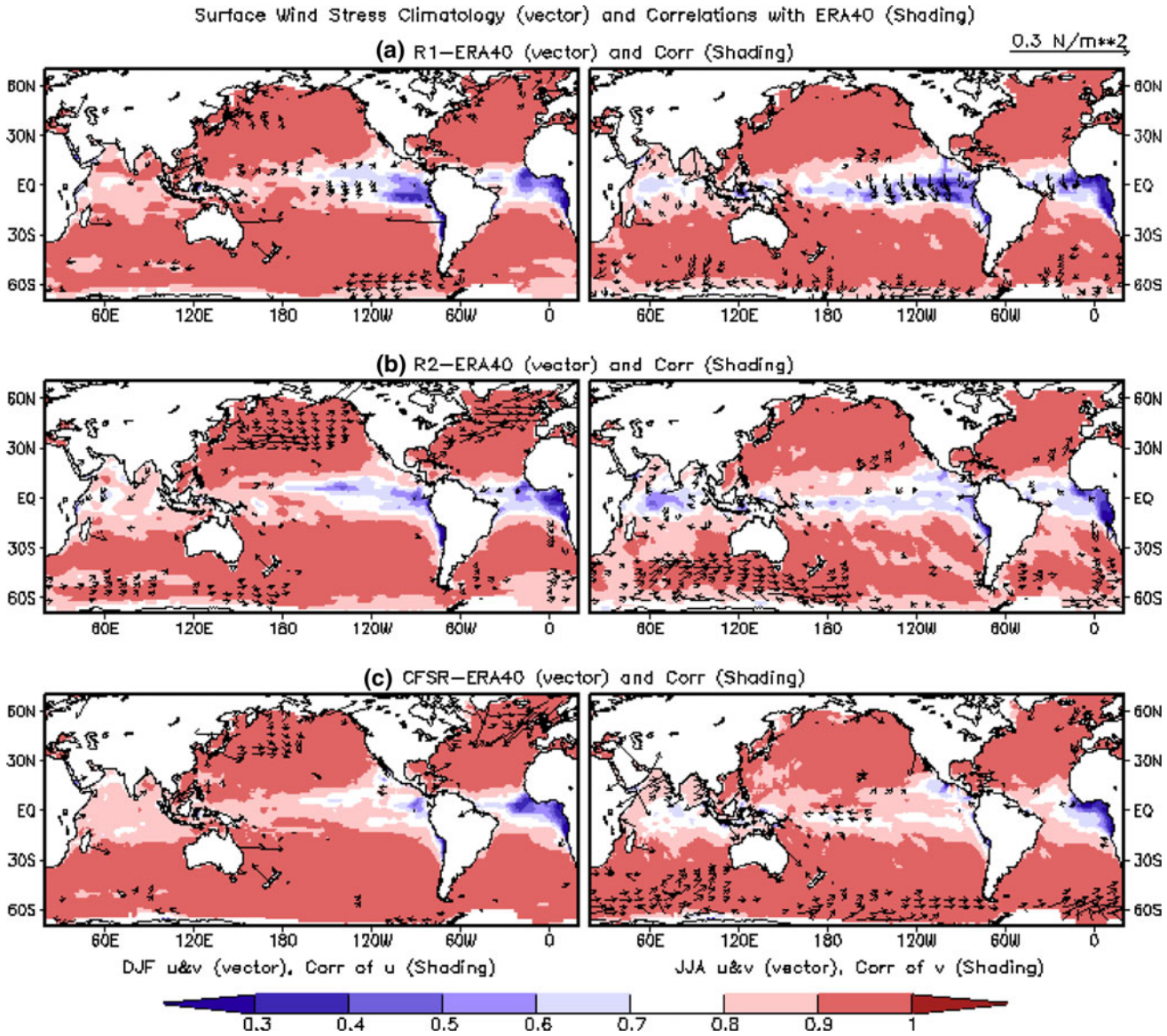

Fig. 3 Comparison of wind stress from the NCEP reanalyses with that from the ERA40 for Dec–Jan–Feb (*left column*) and for Jun–Jul–Aug (*right column*) averaged over the years 1979–2001. Difference vectors (N/m^2) are shown if their amplitudes exceed 0.015 N/m^2. Anomaly correlations (*shading*) are shown for the zonal component (*left column*) and for the meridional component (*right column*). The comparisons are for **a** R1, **b** R2, and **c** CFSR

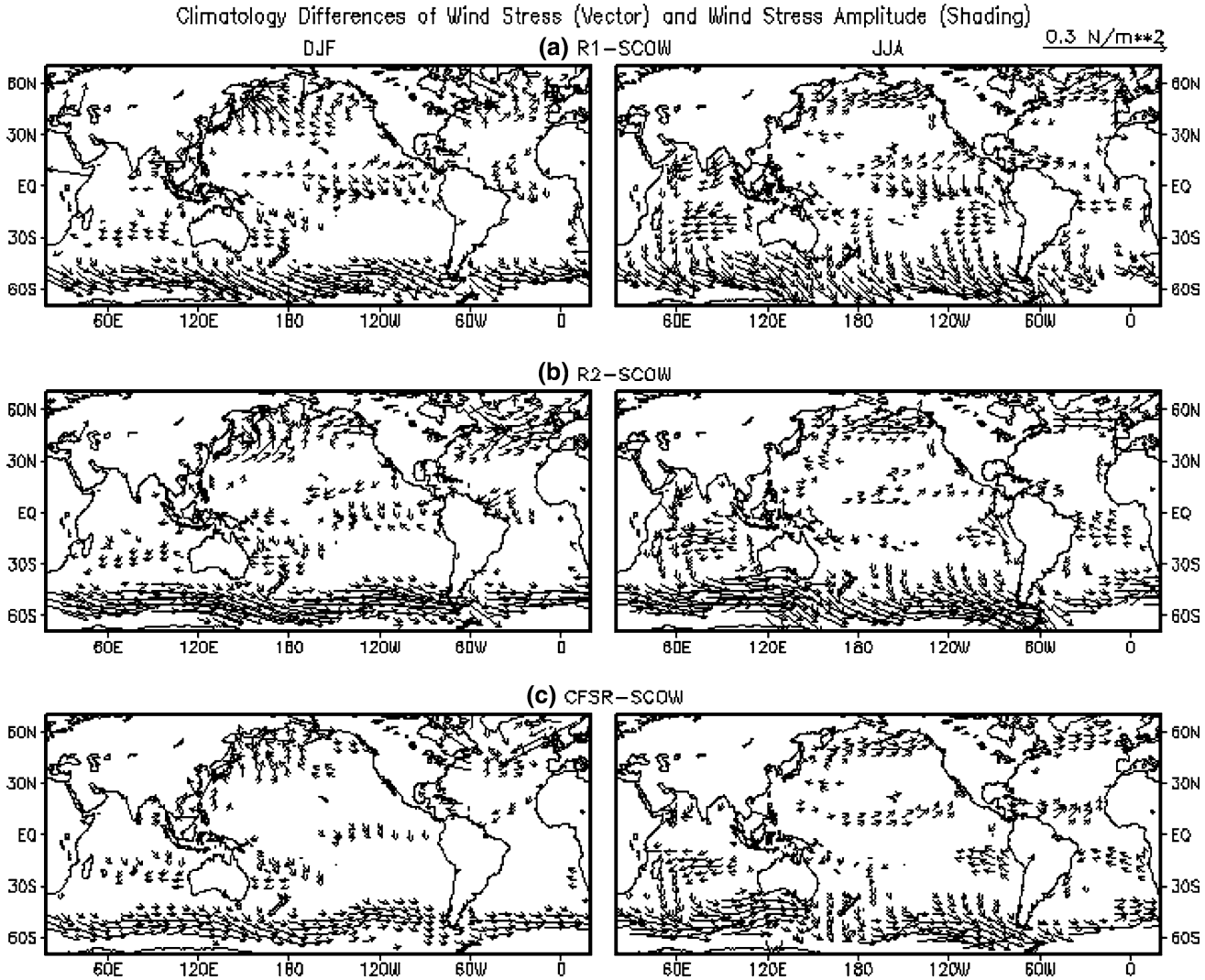

Fig. 4 Comparison of wind stress from the NCEP reanalyses with that from the QuickScat SCOW for Dec–Jan–Feb (*left column*) and for Jun–Jul–Aug (*right column*) for September 1999–October 2009. Difference vectors (N/m^2) are shown if their amplitudes exceed 0.015 N/m^2. The comparisons are for **a** R1, **b** R2, and **c** CFSR

of the climatology from the SCOW and R1, and their comparison results are similar to ours. The climatology differences from the SCOW for R1, R2 and CFSR show some common bias patterns. Compared to the SCOW, the reanalysis westerly wind stress in the high-latitude southern oceans are all too strong; the easterly (southeasterly) wind stress in the subtropical southern Indian and Atlantic Ocean (in the subtropical southeastern Pacific) are all too strong during summer; the westerly wind stress in the high-latitude North Pacific and North Atlantic are all too strong during summer. The differences may be partially caused by the differences in the definition of wind stress. The QuikSCAT wind stress is the true wind stress on the sea surface, taking account the difference between the wind velocity and the surface velocity of the ocean, while the reanalysis wind stresses does not account for the effects of surface ocean currents. In addition, the differences in the bulk algorithms also contribute to the differences. The QuickSCAT wind stress is converted from equivalent neutral-stability 10-m winds using the Large and Pond neutral stability drag coefficient (Risien and Chelton 2008), while the R1, R2, CFSR and ERA40 wind stress use the drag coefficient derived with modified Charnock formula and empirical stability functions. Detailed descriptions of the bulk algorithms in the NCEP and ECMWF models can be found in Renfrew et al. (2002). The equation for momentum roughness length is the same for the R1, R2 and CFSR, but the thermal roughness length in the R1 and R2 has been found to be inappropriate under strong wind conditions and to overestimate LHF (Zeng et al. 1998). The thermal roughness formula of Zeng et al. (1998) is implemented into the NCEP operational model as of 15 June 1998

(Hua-Lu Pan, personal communication), so it is used in the CFSR. Also note that the ERA40 contains wave-induced stress through a coupled ocean-wave, atmosphere model (Perter Janssen, personal communication).

To illustrate the differences in the time evolution of different reanalysis winds, the TAUX averages over several regions are shown in Fig. 5. It is seen in Fig. 5a that the TAUX average in the NINO4 region (160°E–150°W, 5°S–5°N) from the R2 agrees with that from the ERA40 very well, while the TAUX is too weak in the R1 and too strong in the CFSR before 1999. However, TAUX converges in late 1990s when a large amount of satellite data is assimilated (Saha et al. 2010). The easterly wind bias in the CFSR prior to 1999, and the reduction of the bias after 1999, is shown clearly in Table 1. We note that the easterly winds in the ERA40, R1 and R2 strengthened by 50, 61 and 33% from 1979–1998 to 1999–2001, while those in the CFSR strengthened by only 15% largely because of too strong easterly winds in the early period. We will further analyze uncertainties in the equatorial Pacific winds in the CFSR and their impacts on the quality of the equatorial temperature analysis using the TAO data in Sect. 4.4.

In the eastern tropical Pacific, the TAUX in the R1 is too weak, while TAUX agrees well with each other for the other reanalyses (Fig. 5b). In the equatorial Indian Ocean, the TAUX in the CFSR agrees well with other reanalyses mostly during the strong easterly wind events (Fig. 5c). The TAUX in the equatorial Atlantic is about 0.01 N/m^2 stronger in the CFSR and R2 than those in the R1 and ERA40 (Fig. 5d). In the northern oceans, the TAUX in the R2 is too strong, and the other three products agree with each other well (Fig. 5e, f). In the high-latitude southern oceans, the westerly winds from the R1 and R2 have a clear upward trend, while those from the ERA40 and CFSR do not (Fig. 5g). The average of TAUX over the global ocean is positive, with the largest (smallest) value in the R2 (R1) and the values in the CFSR and ERA40 close to each other (Fig. 5h). Overall, CFSR is closer to ERA40 than R1 or R2.

4.2 SST, SSS, and mixed layer depth

4.2.1 SST

During the assimilation, the temperature at 5 m, also referred to as the model SST, is strongly nudged to the

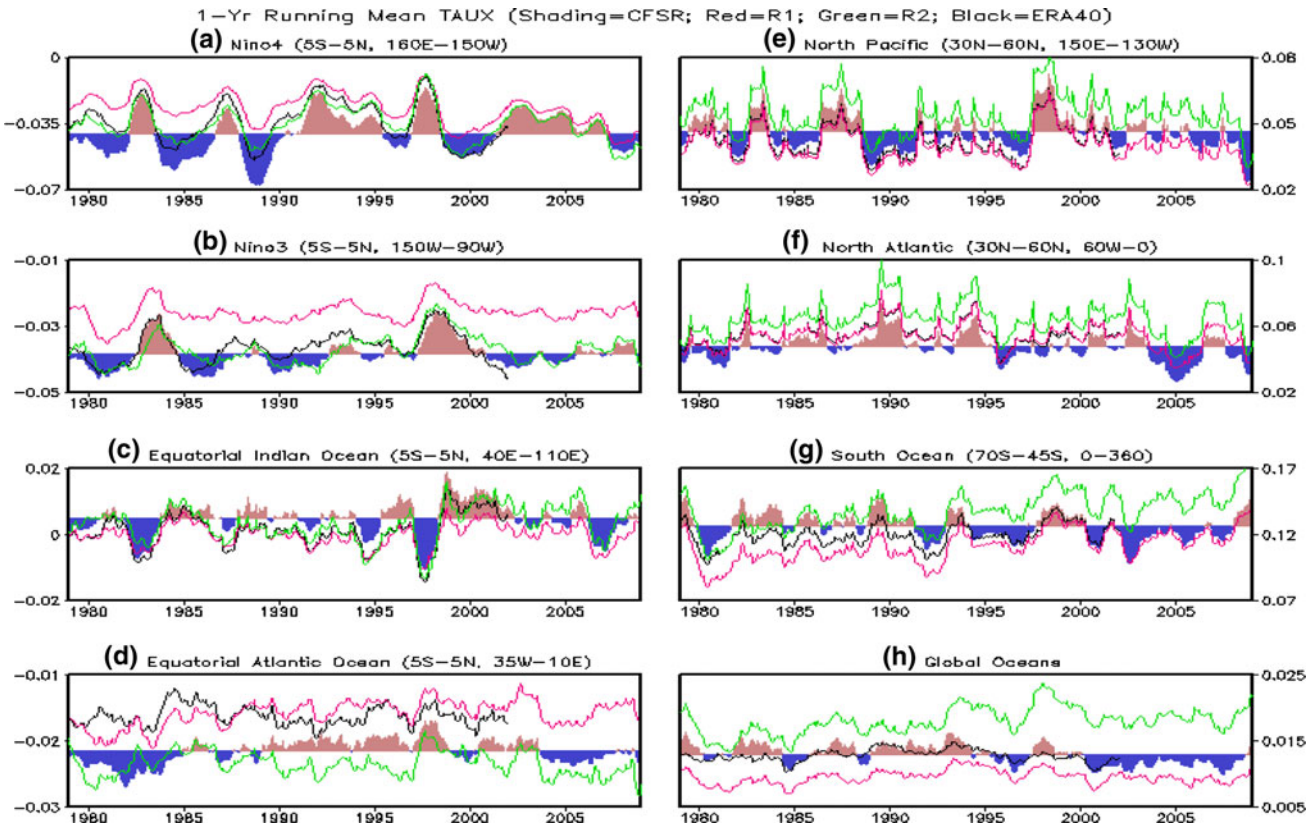

Fig. 5 Time series of 1-year running mean of zonal wind stress in several regions for CFSR (*shading*), R1 (*red line*), R2 (*green line*) and ERA40 (*black line*). Unit is N/m^2. **a** Nino4 (5°S–5°N, 160°E–150°W), **b** Nino3 (5°S–5°N, 150°W–90°W), **c** Equatorial Indian Ocean (5°S–5°N, 40°E–110°E), **d** Equatorial Atlantic Ocean (5°S–5°N, 35°W–10°E), **e** North Pacific Ocean (30°N–60°N, 150°E–130°W), **f** North Atlantic Ocean (30°N–60°N, 60°W-0), **g** Southern Ocean (70°S–45°S), **h** Global Ocean

Table 1 Comparison of zonal wind stress in the NINO4 region (160°E–150°W, 5°S–5°N) in R1, R2, CFSR with that in ERA40 averaged in 1979–1998 and 1999–2001, and differences in the averages

	ERA40	R1	R1-ERA40	R2	R2-ERA40	CFSR	CFSR-ERA40
79–98	−0.32	−0.23	**+0.09**	−0.33	−0.01	−0.41	**−0.09**
99–01	−0.48	−0.37	**+0.11**	−0.44	+0.04	−0.47	+0.01
99–01 to 79–98	**−0.16**	**−0.14**	+0.02	**−0.11**	+0.05	−0.06	**+0.1**

Unit is dyn cm^{-2}

daily OI SST (Reynolds et al. 2007). Wang et al. (2010) showed that the mean CFSR SST is about 0.05–0.1°C warmer than the daily OI SST in the tropical Indian Ocean, the western tropical Pacific and tropical North Atlantic, and they propose the warm SST biases are largely due to too strong SW in those regions. Since the weekly OI SST (Reynolds et al. 2002) has been widely used by research and operational community, and it has been used in validation of the GODAS SST, it is useful to know how well the CFSR SST compares with the weekly OI SST. Overall, the CFSR SST is about 0.2–0.4°C colder than the weekly OI SST except near the western boundary currents. In contrast, the GODAS SST has departures as large as 1°C in the equatorial upwelling regions, southern high latitudes, and near the western boundary currents. In terms of anomaly correlation and root-mean-square differences (RMSDs), the CFSR SST is also superior to the GODAS SST. The anomaly correlation of the CFSR SST is above 0.8 over most of the global ocean, except near the western boundary currents, in the Bay of Bengal and mid- and high-latitude southern oceans. The RMSDs are mostly less than 0.3°C except over the western boundary currents.

4.2.2 SSS

SSS plays an important role in many oceanic processes such as Atlantic Meridional Overturning Circulation (AMOC), the formation of Barrier Layer in the surface layer of the tropics (Sprintall and Tomczak 1992) and hence the mixed layer depth (Lukas and Lindstrom 1991; de Boyer Montegut et al. 2007). SSS variations may also be important in affecting ENSO variability, most notably in the western Pacific where heavy precipitation leads to the formation of a thin mixed layer.

In the CFSR, the salinity at 5 m is nudged to the annual mean SSS from the WOD1998. However, an error in setting the nudging coefficient led to a too strong damping in the model SSS that essentially eliminated both seasonal and interannual variability in SSS.

The climatology of SSS and its seasonal variation in the CFSR and GODAS is compared with those from the WOA05 (Fig. 6). The mean SSS in boreal winter (DJF) and changes in SSS from boreal winter to summer (JJA) shown in Fig. 6a, d, is consistent with those discussed by Levitus (1986). Compared to the WOA05, the CFSR SSS is too low near the Amazon River discharge region, and along the eastern coast of China, Russia and North America (Fig. 6b), which is largely attributable to the inclusion of river runoff in MOM4. Without river runoff, the GODAS SSS is too high near the Amazon River discharge region and the Gulf of Guinea, in the Bay of Bengal, along the eastern coast of China, Russia and North America (Fig. 6c). The seasonal change in SSS is well simulated by the GODAS (Fig. 6f), but, due to a too strong nudging to the annual mean SSS, the seasonal change is absent in the CFSR (Fig. 6e).

4.2.3 MLD

A global climatology of mixed layer depth (MLD) has been constructed based on individual temperature and salinity profiles (de Boyer Montegut et al. 2007). Here we estimate the climatology of MLD based on the annual climatology of temperature and salinity using a criterion of density difference of 0.25 kg m^{-3} between the surface and depth of MLD.

The climatological MLD derived from the WOA05 shows that the MLD in boreal winter (DJF) (Fig. 7a) is larger than 100 m in the central North Pacific, and larger than 200 m in the high-latitude North Atlantic. MLD is generally shallow in the Summer Hemisphere and in the upwelling regions such as the eastern tropical Pacific and tropical Atlantic (Fig. 7a, d). Compared to the MLD of the WOA05, the MLD in the CFSR and the GODAS is about 10–20 m deeper over a large portion of the tropics (Fig. 7b, c, e, f). This is likely related to an underestimation of the barrier layer which is quasi-permanent in the western tropical Pacific and Atlantic, the Bay of Bengal, and the eastern tropical Indian Ocean (de Boyer Montegut et al. 2007). The departures of the CFSR and GODAS from the WOA05 are generally large in mid- and high-latitude southern oceans. The possible reasons for the differences include uncertainties in surface fluxes, and deficiencies in model physics. Note that the WOA05 climatology is calculated with very sparse observations in the southern oceans, while the CFSR and GODAS climatology is based on monthly data for the period 1982–2004.

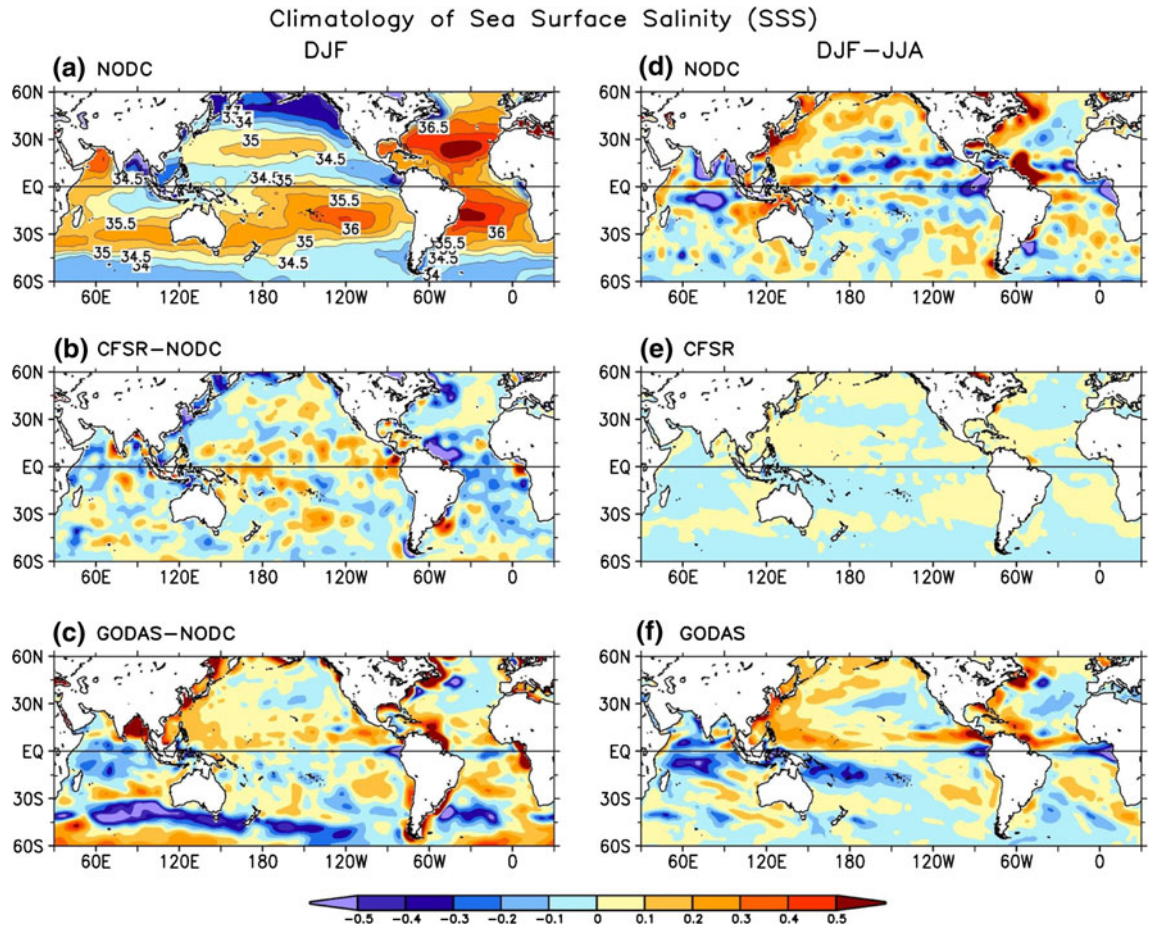

Fig. 6 Sea surface salinity (SSS, salinity at 5 m) for Dec–Jan–Feb (DJF) (*left column*) and seasonal differences between Dec–Jan–Feb (DJF) and Jun–Jul–Aug (JJA) (*right column*). **a**, **d** The NODC climatology from the World Ocean Atlas 2005, **b** CFSR–NODC difference and **e** the CFSR seasonal difference, **c** the GODAS–NODC difference and **f** the GODAS seasonal difference. The average SSS fields for the CFSR and GODAS are for the 1982–2004 period. Unit is practical salinity unit

4.3 Upper ocean heat content and SSH

4.3.1 Upper ocean heat content

Estimation of upper ocean heat content (UOHC) using ocean data assimilation systems can be affected by many factors including uncertainties in surface forcings, ocean model biases, limitations of data assimilation methods, and changes in the input data (Carton and Santorelli 2008). Alternative methods for estimating UOHC are objective analyses that use in situ data only (e.g. Levitus et al. 2009) or combine satellite SSH measurement with in situ data (e.g. Willis et al. 2004). The UOHC in the top 700 m is often used as an indicator of the warming of global oceans due to anthropogenic causes (e.g. Levitus et al. 2009) and represents the thermosteric contribution to sea level rise (e.g. Kohl and Stammer 2008). However, the UOHC in the top 300 m (HC300) is more often used in validation of operational ocean analysis (Xue et al. 2010).

The linear trends of HC300 in 1993–2008 for NODC, CFSR and GODAS are shown in Fig. 8a, b, c. The trend of the NODC shows an increasing (decreasing) HC300 in the western tropical Pacific (in the eastern tropical and subtropical Pacific). The increasing HC in the central North Pacific, and a decrease south of Alaska and off the west coast of North America, is consistent with an overall downward trend in the PDO index (Mantua et al. 1997). An increase in the subpolar North Atlantic is related to the weakening of the subpolar gyre since 1995 (Hakkinen and Rhines 2004). A weak increasing trend exists in the tropical Indian and Atlantic Oceans, and mid-latitude southern oceans. The trend of HC300 is simulated well by the CFSR except in the tropical Indian and Atlantic, and in the eastern equatorial Pacific (Fig. 8b). The GODAS reproduces trends in various ocean basins except in the tropical Indian, and mid- and high- latitude southern oceans (Fig. 8c) where observations are very sparse.

Time series of the HC300 anomaly (HC300a) averaged over selected regions, drawn as boxes in Fig. 8, are

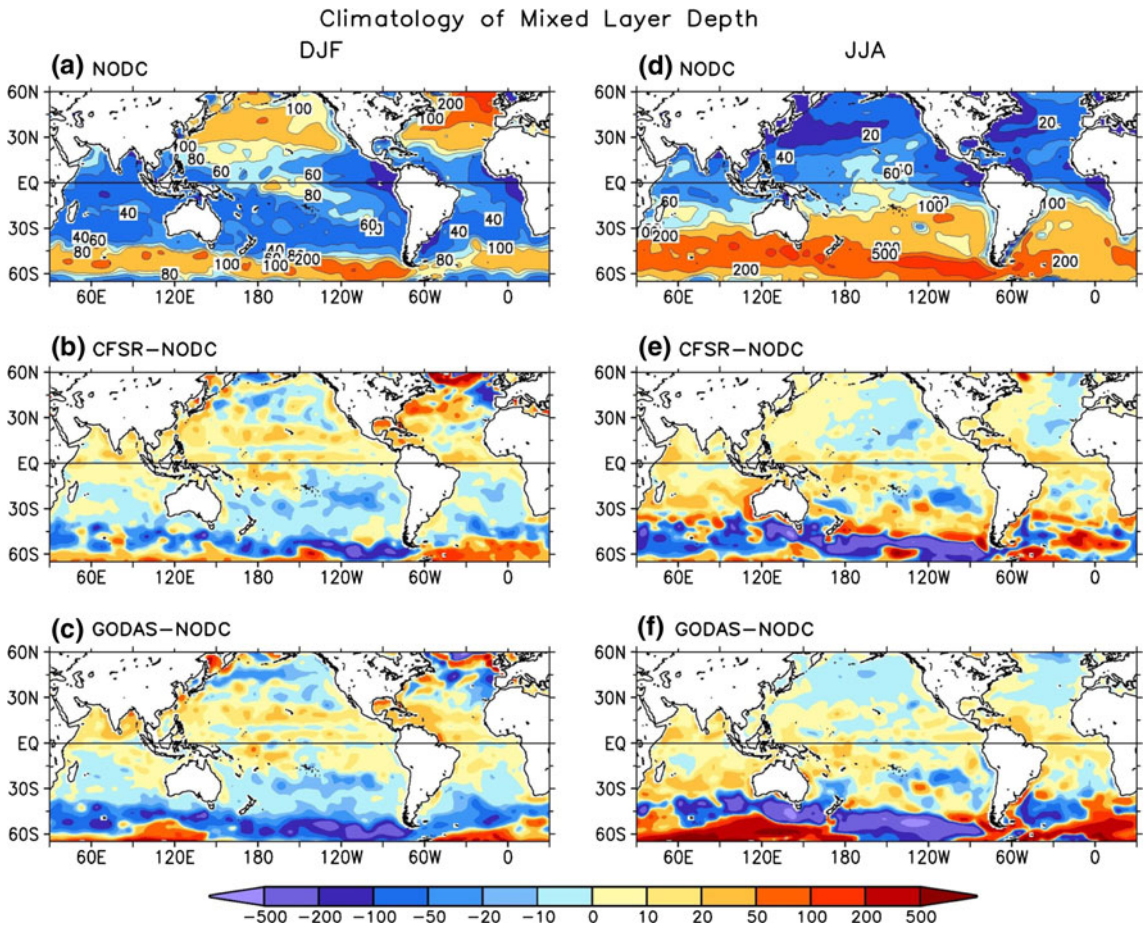

Fig. 7 The mixed layer depth (MLD) for Dec–Jan–Feb (DJF) (*left column*) and for Jun–Jul–Aug (JJA) (*right column*). The MLD is calculated using a criterion of a density difference of 0.25 kg/m^3 between the surface and the base of the MLD. The NODC climatology is based on the World Ocean Atlas 2005, and the averages for the CFSR and the GODAS are for the 1982–2004 period. Unit is m. **a**, **d** NODC, **b**, **e** CFSR–NODC, **c**, **f** GODAS–NODC

displayed in Fig. 9. Both the CFSR and GODAS agree very well with the NODC in the tropical western Pacific, the central North Pacific and the high-latitude North Atlantic where an upward HC300a trend is prominent (Fig. 9a, d, g). In the equatorial eastern Pacific (Fig. 9b), HC300a is dominated by interannual variability. We note that the GODAS agrees with the NODC, but the CFSR has a warmer bias after 1999. We will discuss this issue further in Sect. 4.4. In the subtropical northeast Pacific, both the CFSR and GODAS agree well with the NODC, and have a clear downward trend (Fig. 9e). In contrast, the trend in the subtropical southeast Pacific is very weak (Fig. 9f). The disagreements among the three products are quite large in the equatorial Atlantic (Fig. 9c) and the subtropical North Atlantic (Fig. 9h), consistent with large discrepancies of wind stress in those regions discussed in Sect. 4.1.2. We also note that the global HC300a had a sharp decline from 1991 to 1994, likely due to the volcanic eruption of the Mt. Pinatubo in June 1991 (Fig. 9i). The upward trend of the global mean HC300a is simulated better by the CFSR than by the GODAS. This is because the time that is taken for the model to converge onto observations is shorter in the CFSR than in the GODAS at the beginning of the analysis, and the strong warming trend during the period from 2000 to 2005 is better simulated in the CFSR than in the GODAS (Fig. 9i).

4.3.2 SSH

SSH based on altimetry (Altimetry) provides an independent validation of the HC variability due to its thermostatic contribution. The linear trend of HC300a from the NODC in 1993–2008 is consistent with the linear trend of Altimetry (referred to as AVISO in Fig. 8d) except that the positive tendency in Altimetry is more prominent in mid- and high- latitude southern oceans and in the tropical Atlantic. The trend of SSH anomaly (SSHa) is well simulated by the CFSR in the western tropical Pacific, North Pacific, North Atlantic and high-latitude southern Indian ocean, but it is poorly simulated in the tropical Atlantic,

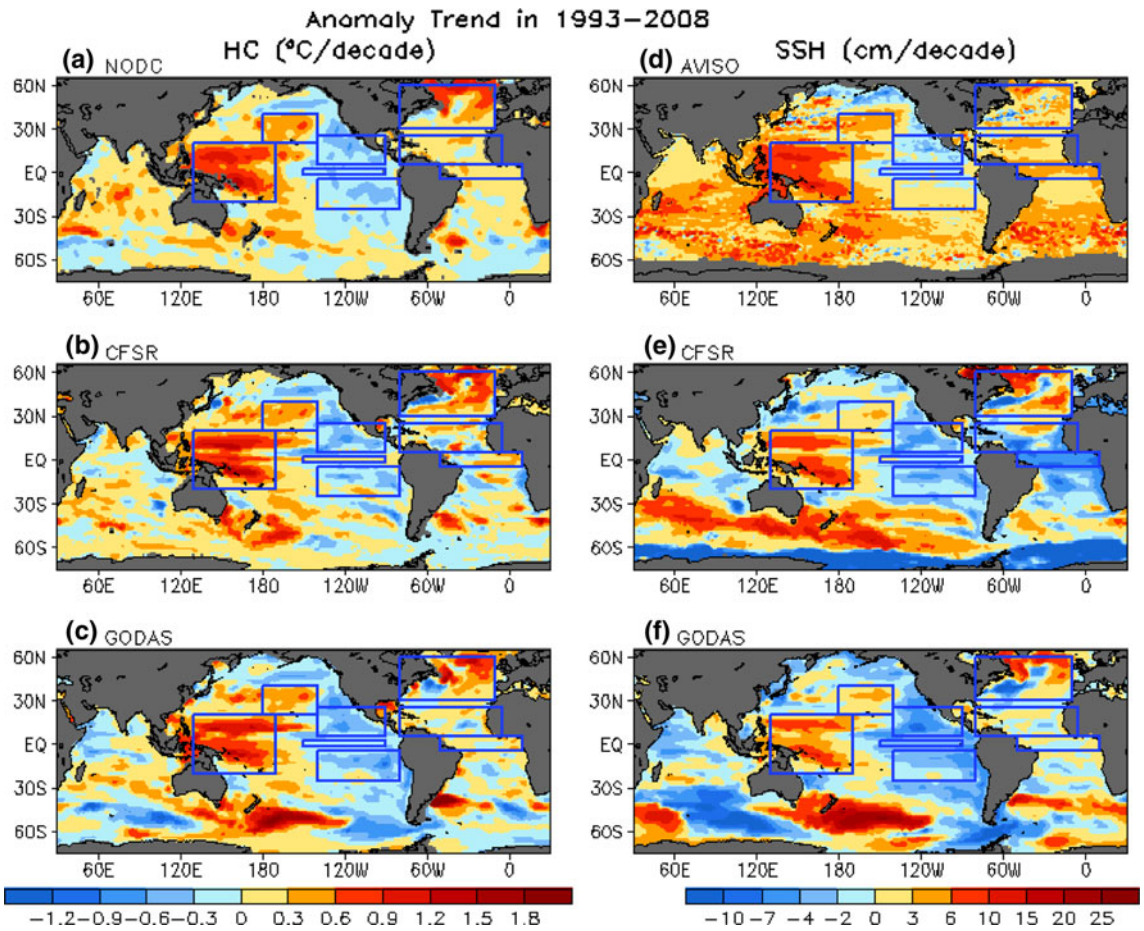

Fig. 8 Linear trend for 1993–2008 in the upper 300 m heat content (HC300, °C/decade) anomaly from **a** NODC, **b** CFSR and **c** GODAS, and in the sea surface height (SSH, cm/decade) anomaly from **d** AVISO, **e** CFSR and **f** GODAS. Time series of the average HC300 anomaly in the *boxes* drawn here are shown in Fig. 9

tropical Indian Ocean, and southeastern tropical Pacific. The GODAS agrees with the Altimetry better than the CFSR in the tropical Atlantic, but worse in the high-latitude southern Indian Ocean.

The correlation of SSHa between the CFSR (GODAS) and the Altimetry, and their differences, are shown in Fig. 10a, b, c. The correlation between the CFSR and Altimetry is high (>0.6) in the tropical and subtropical Pacific, eastern North Pacific, western South Pacific, tropical Indian Ocean and subpolar North Atlantic (Fig. 10a). However, the correlation is low (<0.4) in the western North Pacific, the Atlantic Ocean south of 40°N and most of mid- and high-latitude southern oceans. Compared to the GODAS (Fig. 10b), the CFSR has a higher correlation in the tropical Indian Ocean, extratropical North Pacific and North Atlantic, and high-latitude southern oceans, which are likely attributable to improvements in the surface forcings. However, the correlation in the tropical Atlantic is seriously degraded in the CFSR (Fig.10c).

The RMSD of SSHa between the CFSR (GODAS) and the Altimetry is generally low (<4 cm) in the tropical oceans, but high (>8 cm) near the western boundary currents, and in mid- and high-latitude southern oceans. The CFSR has smaller RMSD than the GODAS in the trpical Indian Ocean, near the Gulf Stream, and in high-latitude southern oceans, but higher RMSD in the tropical Atlantic and near the Antarctic.

4.4 Tropical Pacific

It is critically important to validate the quality of the ocean analysis in the tropical Pacific, since it provides the ocean memory for long-lead seasonal forecasts (Balmaseda et al. 2010). We use the TAO mooring data to validate the subsurface temperature, subsurface currents, and the surface winds, and use the OSCAR analysis to validate the surface currents.

4.4.1 Comparison with TAO temperature profile

Validation at four equatorial TAO moorings at 165°E, 170°W, 140°W, 110°W provide a basin wide assessment

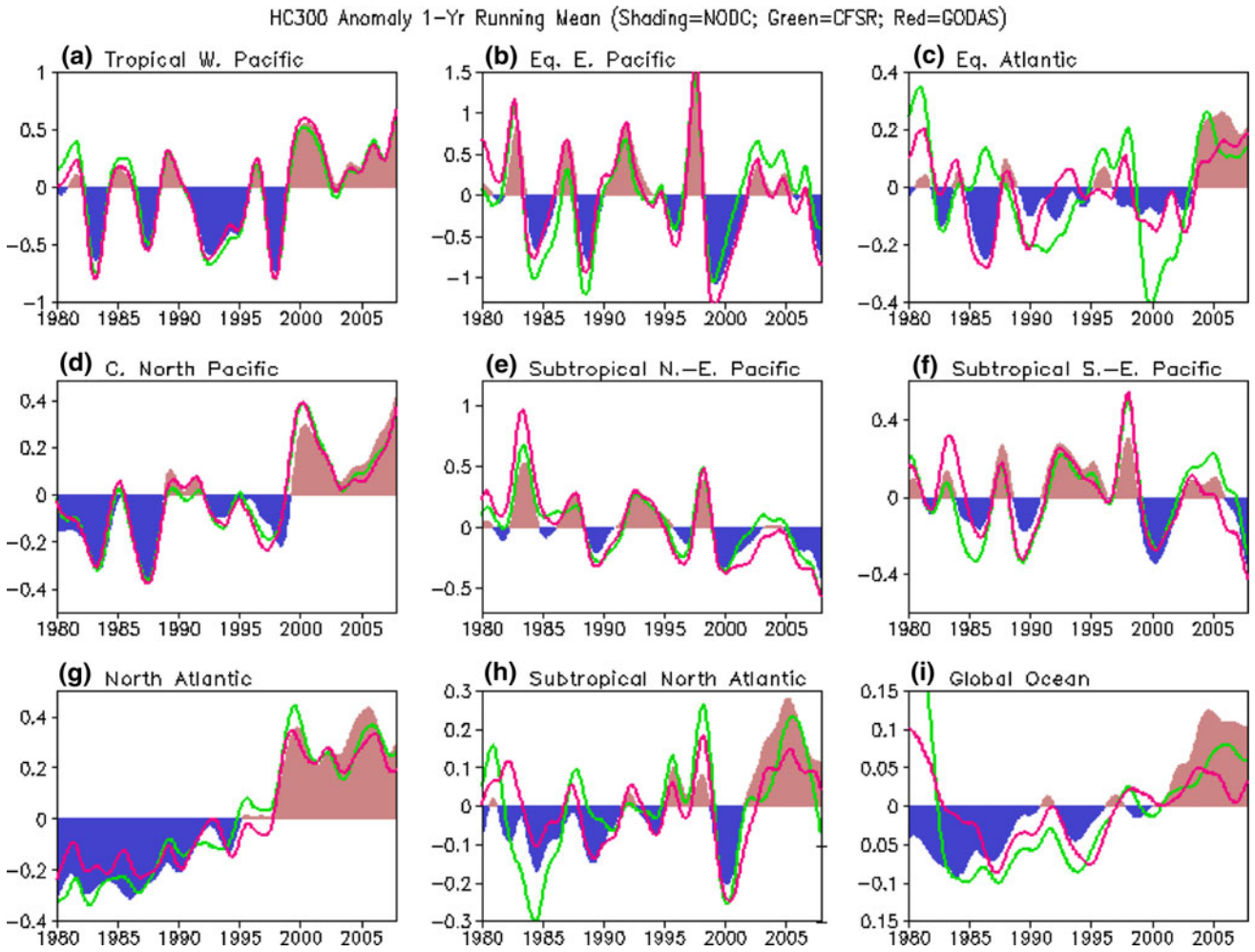

Fig. 9 Time series of one-year running means of the HC300 anomaly averaged in various boxes (refer to Fig. 8 for their locations) for NODC (*shading*), CFSR (*green line*) and GODAS (*red line*). Unit is °C. **a** Tropical western Pacific, **b** equatorial eastern Pacific, **c** equatorial Atlantic, **d** central North Pacific, **e** subtropical northeast Pacific, **f** subtropical southeast Pacific, **g** subpolar North Atlantic, **h** subtropical North Atlantic and **i** Global Ocean

for both the temperature and the velocity, and have been widely used in the validation of ocean analyses (Behringer et al. 1998; Behringer and Xue 2004; Balmaseda et al. 2008).

Figure 11 shows the departures of the CFSR temperature from the TAO temperature as functions of depth and time at the four TAO mooring locations. In the western (165°E) and central (170°W) Pacific, temperature departures are mostly negative at depths below 200 m. In the eastern Pacific (140°W and 110°W), temperature departures are mostly negative before 1999, but become persistently positive after 1999 with amplitude as large as 2°C. This suggests that there is a shift in the quality of the CFSR temperature analysis around 1998/1999.

4.4.2 Comparison with TAO current profile

The velocity measurements from the Acoustic Doppler Current Profilers (ADCP) and Current Meters at the four equatorial TAO mooring sites (165°E, 170°W, 140°W and 110°W) are combined to provide a more complete velocity data set. Keeping the shift in the temperature bias in mind (Fig. 11) we compare the current for the 1979–1998 and 1999–2008 periods separately (Fig. 12). The TAO currents suggest little decadal changes in the two periods, but the CFSR analysis indicates that the surface zonal currents in the central and eastern Pacific increased by more than 40 cm/s from the early to later period. The GODAS currents are generally superior to the CFSR currents in the central and eastern Pacific (170°W, 140°W, 110°W), but inferior in the western Pacific (165°E). The vertical average of anomaly correlation in 1979–2008 between the CFSR (GODAS) and TAO is 0.41 (0.33), 0.45 (0.59), 0.57 (0.58), and 0.52 (0.53), and the RMSD is 26 (29 cm/s), 27 (22 cm/s), 30 (23 cm/s), and 31 cm/s (27 cm/s) at the four sites, respectively.

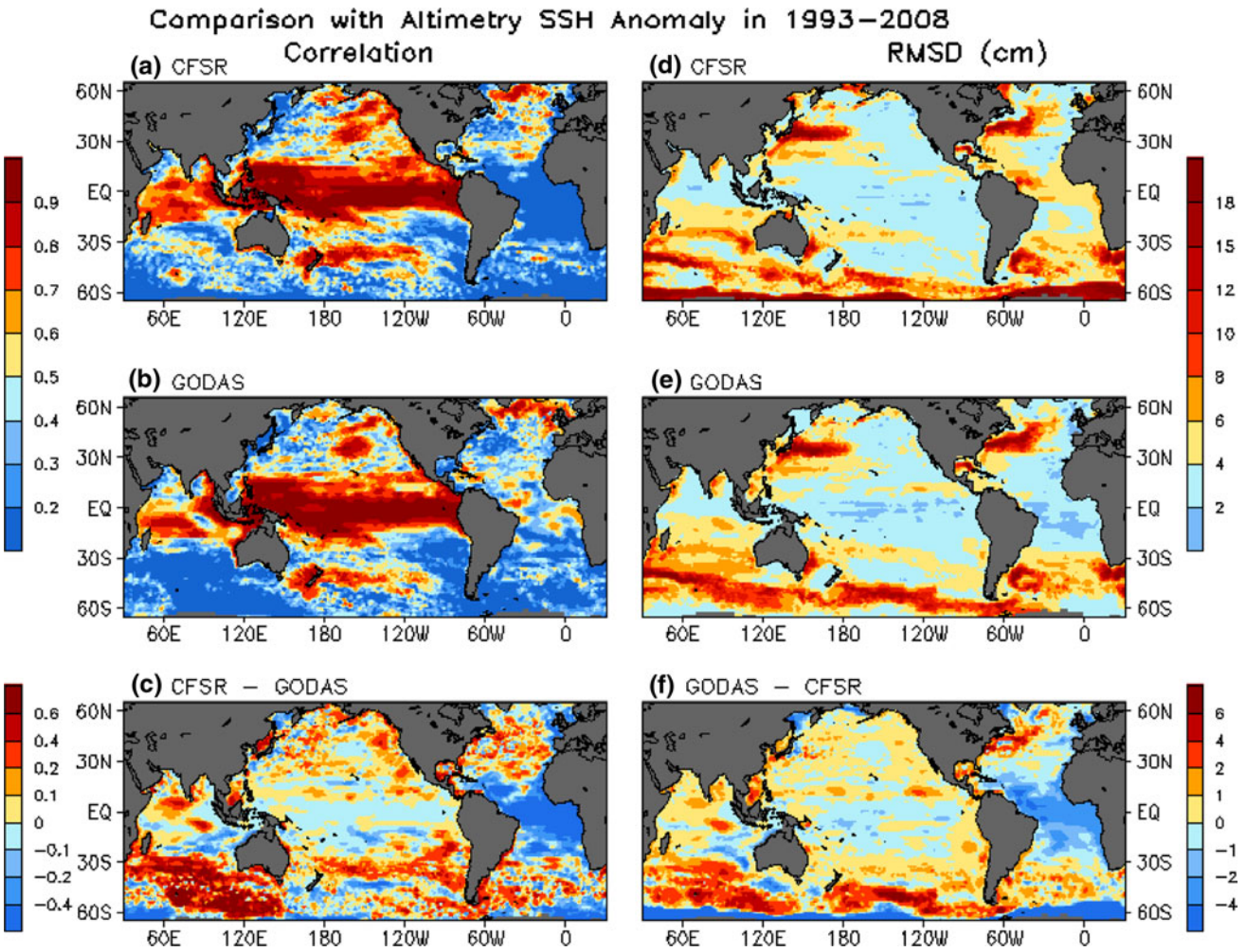

Fig. 10 Anomaly correlations of SSH from **a** the CFSR and **b** the GODAS with the AVISO altimetry, and **c** difference between the CFSR and GODAS correlations; Root-mean-square difference (RMSD) of the SSH anomaly (cm) of **d** the CFSR and **e** the GODAS with the AVISO altimetry, and **f** difference between the GODAS and CFSR RMSDs. The global average of the anomaly correlation between the CFSR (GODAS) SSH and the AVISO altimetry is 0.45 (0.44) and of the RMSD between the CFSR (GODAS) and the AVISO altimetry is 4.9 cm (4.7 cm)

4.4.3 Comparison with OSCAR surface currents

The surface zonal currents (SZCs) in the CFSR and GODAS are validated against the OSCAR currents, which measures the average currents in the top 30 m. Figure 13 shows the comparison of the SZC averaged within the box 160°E–120°W, 2°S–2°N for the OSCAR, CFSR and GODAS. The mean SZC are calculated separately for the period 1979–1998 and 1999–2008 for the GODAS and CFSR, and for the period 1993–1998 and 1999–2008 for the OSCAR. It is interesting that the means of the OSCAR ZSC in the two periods are indistinguishable, while the means of the GODAS SZC and the CFSR SZC are different in the two periods. Figure 13b indicates that the mean SZC in the GODAS agrees well with that in the OSCAR in 1979–1998, but has a positive bias of about 18 cm/s during the period 1999–2008. In contrast, the mean SZC in the CFSR (Fig. 13a) has a negative bias of 10 cm/s in 1979–1998, and a positive bias of 30 cm/s in 1999–2008. For the whole period 1979–2008, the anomaly correlation between CFSR (GODAS) and OSCAR is 0.61 (0.82), and the RMSD between CFSR (GODAS) and OSCAR is 31 cm/s (20 cm/s), indicating the GODAS SZC is superior to the CFSR SZC.

The positive biases in the CFSR SZC since 1999 are related to the warm biases in the equatorial temperature during the same period (Fig. 11). On the equator, the zonal currents are maintained by a balance between the east–west pressure gradient, the easterly winds and friction. As a possible explanation (1) the easterlies did not increase as much as observed at the end of 1998 when the ATOVS data was assimilated (Tables 1, 2), (2) so the slope of the thermocline did not increase as much as observed due to the weaker strengthening of easterlies, (3) the assimilation

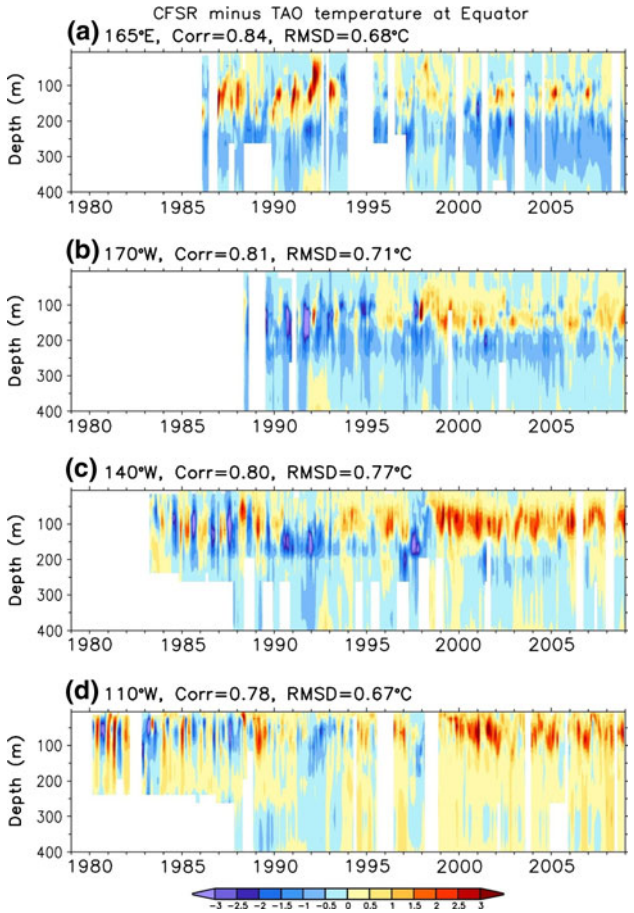

Fig. 11 Differences between CFSR and TAO temperature (°C) at four equatorial TAO mooring sites at **a** 165°E, **b** 170°W, **c** 140°W, and **d** 110°W for the period 1979–2008. The vertical average of the anomaly correlation between CFSR (GODAS) and TAO is 0.84 (0.90), 0.81 (0.91), 0.80 (0.88), and 0.78 (0.85) at the four sites, respectively, while the root-mean-square difference (RMSD) between CFSR (GODAS) and TAO is 0.68°C (0.49°C), 0.71°C (0.43°C), 0.77°C (0.61°C), and 0.67°C (0.64°C), respectively

of TAO temperature data help increase the slope (but not enough to avoid a shift in the temperature bias), (4) the east–west pressure gradient, increased by the assimilation, is not in balance with the too-weak easterlies, (5) and so the currents accelerate to the east until the stress-pressure gradient-friction balance is restored.

4.4.4 Comparison with TAO surface winds

To further understand the causes for the warm biases of the subsurface temperature in the CFSR (Fig. 11), we estimate the uncertainties in the surface winds in the CFSR using the TAO winds at the four equatorial mooring sites (Table 2). The mean biases of the CFSR from the TAO are easterlies in the western (165°E) and central (170°W) Pacific in 1979–1998, which is consistent with the comparison result with the ERA40 (Table 1). It is interesting to note that the easterly winds in the TAO strengthened by 1–2 m/s in the west-central Pacific (165°E, 170°W) from the early to the later period. However, the strengthening of the easterly winds is severely underestimated by CFSR, largely due to its overestimation of the easterly winds in the early period (Table 2). The underestimation of the strengthening of the easterly winds has a significant impact on the equatorial temperature analysis, which is discussed in the next section.

Since GODAS does a good job in simulating the HC300a in the western and eastern tropical Pacific (Fig. 9a, b), it is interesting to check if the R2 winds, which are used to force the GODAS, agree with the observations better than the CFSR winds. Table 2 shows that the biases in the R2 zonal winds are indeed smaller than those in the CFSR zonal winds. More importantly, the R2 realistically simulates the strengthening of the easterly winds in the central Pacific, which plays a dominant role in forcing the linear trend of HC300a in the western and eastern tropical Pacific (Fig. 8a, c).

We also estimated uncertainties of the meridional winds in the CFSR and R2 (Table 3). The CFSR overestimates the strength of the mean meridional winds at 140°W (110°W) by more than 100% (42%). The CFSR has a large positive bias at 170°W in 1999–2008, which switches the original northerly winds into southerly winds. The mean biases in the R2 are generally smaller than those in the CFSR, except they are very large in the western Pacific in 1979–1998.

4.4.5 Explanation of the eastern Pacific warm bias in the CFSR since 1999

The underestimation of the strengthening of the easterly winds in the CFSR around 1998/1999 provides a simple explanation for the sudden shift in the equatorial temperature bias in the CFSR (Fig. 11). In the real world, in response to the strengthening of the easterlies, the thermocline became deeper in the west and shallower in the east. In the CFSR, the increase in the easterlies is significantly less than that in observations, largely due to the easterly wind bias prior to 1998, so the mean slope of the thermocline remained largely unchanged. The effect on the temperature bias in the CFSR would be largest in the thermocline and the bias would become colder in the west and warmer in the east. This is exactly what we see in Fig. 11, as the bias shifts to colder values at 165°E, while east of the dateline the bias shifts to warmer values and becomes warmest at the two most eastern sites, 140°W and 110°W.

4.5 Drifts in the equatorial temperature and salinity

The climatology of the equatorial temperature and salinity, calculated from the seasonal NODC temperature for

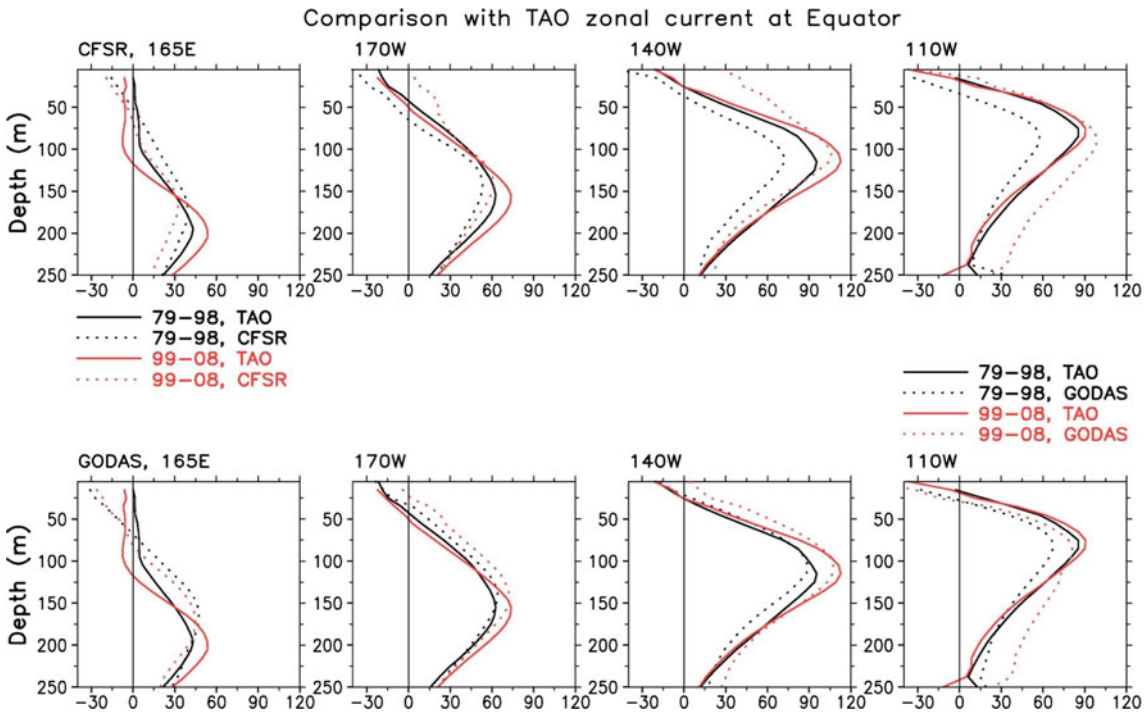

Fig. 12 Comparison of the mean zonal current (cm/s) of CFSR (*upper row*, *dotted line*) and GODAS (*lower row*, *dotted line*) with the TAO current (*solid line*) at four equatorial mooring sites at 165°E, 170°W, 140°W, and 110°W for two periods, 1979–1998 (*black*) and 1999–2008 (*red*). Note that only the periods when both the CFSR (GODAS) and TAO data were available were included in calculation of the means. The vertical average of the anomaly correlation for the period 1979–2008 between CFSR (GODAS) and TAO is 0.41 (0.33), 0.45 (0.59), 0.57 (0.58), and 0.52 (0.53) at the four sites, respectively, while the root-mean-square difference (RMSD) between CFSR (GODAS) and TAO is 26 (29 cm/s), 27 (22 cm/s), 30 (23 cm/s), and 31 cm/s (27 cm/s), respectively

1979–2008 and the 5-year mean NODC salinity for 1979–2004, is shown in Fig. 14a, d. In the climatology, the thermocline, where the vertical gradient of temperature is largest, slopes upward from west to east in the equatorial Pacific and Atlantic, while in the equatorial Indian Ocean slopes downward from west to east. The CFSR temperature has a negative (positive) bias of about 0.5°C near the thermocline in the central (far western) Pacific in 1979–1998, while it has a positive bias of more than 1°C near the thermocline in the central-eastern Pacific and 0.5°C below 200 m in the eastern Pacific in 1999–2008 (Fig. 14b, c). The CFSR temperature has a positive bias of 1°C in the equatorial western Indian Ocean and the equatorial Atlantic.

The mean salinity in the equatorial Pacific is characterized by fresh water (less than 34.8 psu) in the top layer in the western and far eastern Pacific and at the depths below 400 m, and saline water (more than 35.2) beneath the fresh water in the western Pacific extending eastward and upward to near the surface in the central Pacific (Fig. 14d). Saline water presents in the west-central Indian Ocean, with fresh water in the far eastern Indian Ocean. The equatorial Atlantic is much saltier than the other two ocean basins in the top 300 m. The CFSR salinity has negative biases of 0.3 psu in the equatorial eastern Indian Ocean. In the equatorial Pacific, CFSR salinity agrees well with the NODC salinity in 1979–1998, but it has negative biases of 0.5 psu near the thermocline and positive biases of 0.1 psu below 400 m in 1999–2004 (Fig. 14e, f). The CFSR salinity biases are largest in the equatorial Atlantic, with a negative (positive) bias of 0.5 psu above 100 m (below 300 m).

Since the CFSR was produced with six data streams (Saha et al. 2010), we examine if there are any discontinuities in the time series. The time evolution of the equatorial temperature and salinity anomalies averaged in each ocean basin is shown in Fig. 15, where the vertical dash lines indicate the times when one stream connects with the subsequent one. In the equatorial Indian Ocean, the temperature in the first stream is much warmer than the second stream, and may be related to a spin up of the ocean model from an initial ocean state in January 1979, which is too warm compared to the initial ocean state in January 1987 at the beginning of the second stream. There is little discontinuity in temperature for the other streams. It is worthwhile to point out that the subsurface temperature below 500 m increased substantially around 2003 when the Argo data became available. The positive salinity anomalies in the first and last stream are associated with the positive temperature anomalies due to assimilation of synthetic salinity.

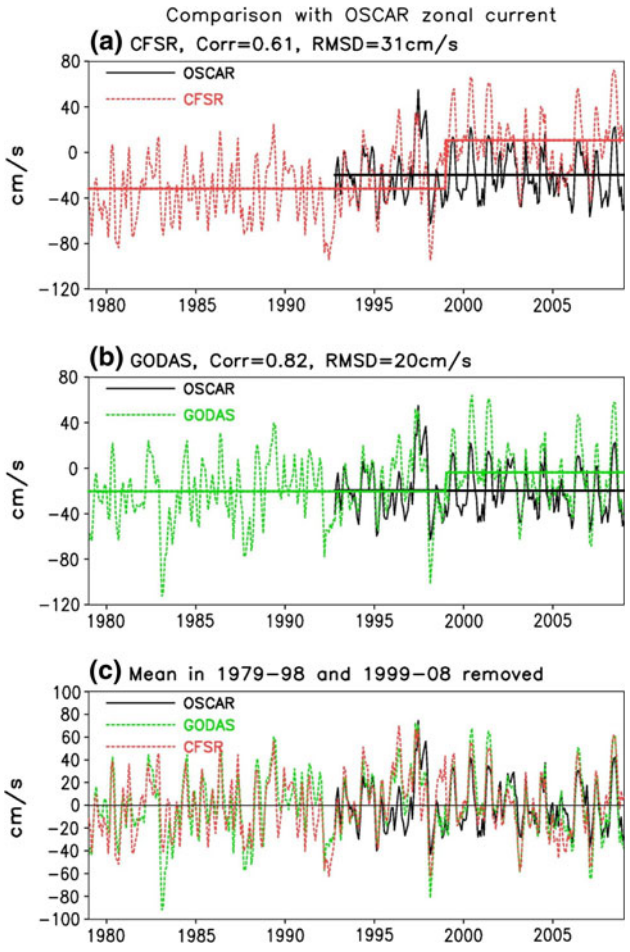

Fig. 13 Comparison of zonal currents averaged within the *box*, 160°E–120°W, 2°S–2°N, **a** CFSR (*red dotted line*) and OSCAR (*black solid line*) with their means prior to 1999 and after 1999 shown as horizontal *thick-solid lines*, **b** GODAS (*green dotted line*), and OSCAR (*black solid line*), **c** GODAS (*green dotted line*), CFSR (*red dotted line*) and OSCAR (*black solid line*) in which their respective means prior to 1999 and after 1999 were removed. The anomaly correlation between CFSR (GODAS) and OSCAR is 0.61 (0.82) and the root-mean-square difference (RMSD) between CFSR (GODAS) and OSCAR is 31 cm/s (20 cm/s)

In the equatorial Pacific, the temperature anomaly in the top 200 m is dominated by interannual variability associated with ENSO prior to 2000, while persistent positive anomalies extend from the surface to at least 900 m from 2000 to 2008. We also note that the subsurface temperature below 200 m increased substantially around 1990 with the availability of the TAO temperature profiles. Associated with the increase of temperature around 1990 is a rapid increase of salinity below 300 m in the early 1990s. Positive salinity anomalies in the top 300 m switched from positive to negative anomalies around 1991, coincident with the switch of salinity anomalies below 300 m.

The discontinuities and drifts in temperature and salinity are largest in the equatorial Atlantic, particularly in the deep ocean (note the differences in units and different scale of *y*-axis). This is associated with the poor simulation of SSHa in the tropical Atlantic (Fig. 10c). It is not clear what factors contribute to the large drifts. Sensitivity experiments need to be done in the future to find out the causes for those drifts.

5 Simulation of climate variability

5.1 Tropical Pacific

5.1.1 Tropical instability wave

Tropical instability waves (TIWs) are commonly observed phenomena in the tropical Pacific and Atlantic, where they appear as westward-propagating wavelike oscillations of the temperature front between cold upwelling equatorial water and warmer water to the north (Duing et al. 1975). The typical zonal wavelength and period of TIWs in the Pacific are about 1,000–2,000 km, 20–40 days (e.g. Qiao and Weisberg 1995). TIWs have been recognized as key elements to equatorial mixed layer heat, momentum budget, and air-sea coupling both from observation and modeling studies (e.g. Hashizume et al. 2001; Jochum and Murtugudde 2006). However, TIWs are not resolved in previous reanalysis datasets. An important issue is how the CFSR reproduces observed TIWs activities.

Two observed SST data are used to validate CFSR performance. One is the daily OI SST (Reynolds et al.

Table 2 Comparison of zonal winds (m/s) of CFSR and R2 at 10 m with those of TAO winds at 4 m at four mooring sites averaged in 1979–1998 and 1999–2008, and differences in the averages

	165°E			170°W			140°W			110°W		
	TAO	CFSR	R2	TAO	CFSR	R2	TAO	CFSR	r2	TAO	CFSR	R2
79–98	−0.7	**−2.1**	**−1.7**	−4.4	**−5.0**	−4.0	−5.6	−5.7	−5.6	−3.7	−3.7	−3.9
99–08	−2.5	−2.8	−2.5	−5.6	−5.4	−5.2	−5.6	−5.5	−5.6	−3.4	−3.7	−3.5
99–08 to 79–98	−1.7	**−0.7**	**−0.8**	−1.2	**−0.4**	−1.2	0.0	+0.2	0.0	+0.3	0.0	+0.4

Numbers are in bold whenever their differences from TAO are larger (less) than +0.5 (−0.5) m/s

Table 3 Same as Table 2 except for the meridional winds

	165°E			170°W			140°W			110°W		
	TAO	CFSR	R2	TAO	CFSR	R2	TAO	CFSR	R2	TAO	CFSR	R2
79–98	−0.64	−0.60	**+0.08**	−0.57	−0.28	−0.50	+0.31	**+1.5**	+0.69	+2.4	**+3.4**	**+3.0**
99–08	−0.48	−0.52	−0.56	−0.45	**+0.19**	**+0.10**	+0.95	**+1.9**	+1.1	+2.5	**+3.5**	**+3.3**
99–08 to 79–98	+0.16	+0.08	**−0.64**	+0.12	+0.47	+0.60	+0.64	+0.4	+0.4	+0.1	+0.1	+0.3

Numbers are in bold whenever their differences from TAO are larger (less) than +0.5 (−0.5) m/s

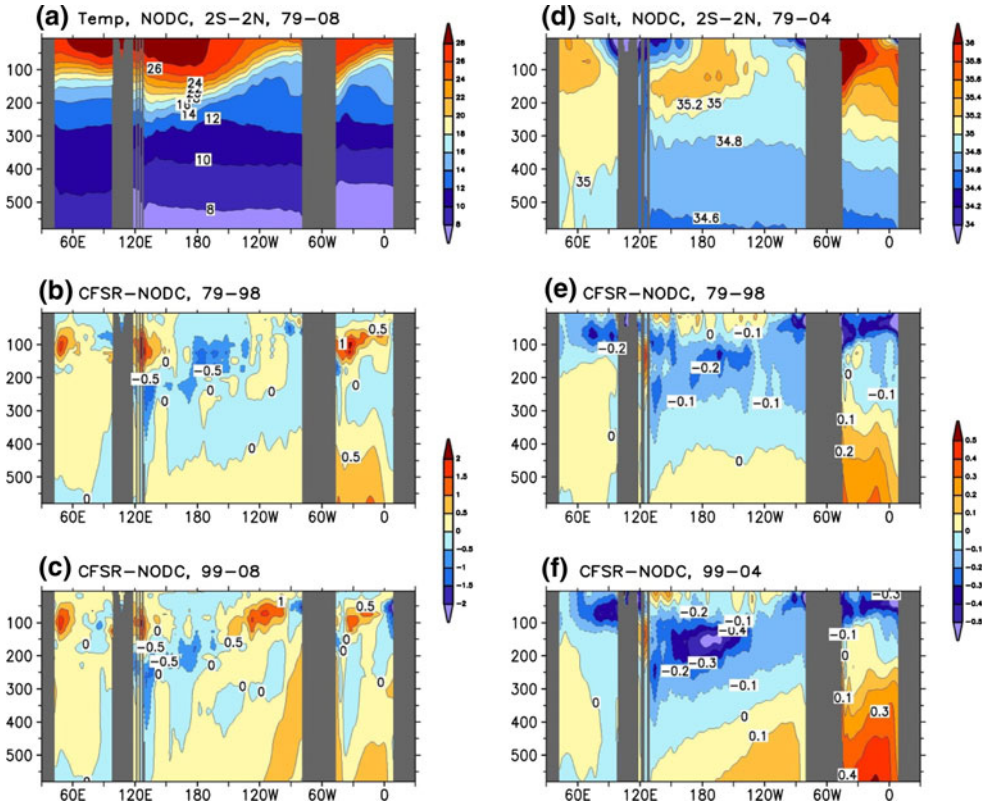

Fig. 14 Average temperature (*left*, °C) and salinity (*right*, psu) in the 2°S–N2°N band for **a** the NODC temperature for the period 1979–2008, **b** the CFSR minus NODC temperature for the period 1979–1998, **c** the CFSR minus NODC temperature for the period 1999–2008, **d** the NODC salinity for the period 1979–2004, **e** the CFSR minus NODC salinity for the period 1979–1998 and **f** the CFSR minus NODC salinity for the period 1999–2004

2007) for the period 1982–2008, the other one is the TRMM Microwave Imager (TMI) SST version 4 from Remote Sensing Systems (RSS) for the period 1999–2008. Both OI SST and TMI SST are originally gridded at a 0.25° × 0.25°. These data sets were regridded to the CFSR 0.5° × 0.5° grid.

In order to extract signals in the TIWs, we apply a bandpass filter to the data at periods of 20–40 days and then isolate the component at zonal wave lengths 900–2,300 km. To facilitate comparison, we define a TIW SST index as the spatial standard deviation of filtered SST over the box 160°W–95°W, 0°N–3°N. Figure 16 shows the evolution of TIW SST indices from the CFSR SST, OI SST and TMI SST. The simulated TIW in the CFSR compares well with the OI SST, which has been used to nudge the model SST. TIWs in the CFSR and the OI SST are both weaker than those in the TMI SST, particularly during 1999–2002. TIWs are weak before 1982, since the monthly HadISST was used to nudge to the model SST.

5.1.2 *Oceanic Kelvin waves*

The episodic easterly and westerly wind anomalies associated with the Madden-Julian Oscillation (MJO), and westerly wind bursts, force upwelling and downwelling oceanic Kelvin waves (OKWs) that cross the equatorial Pacific in about 2 months (Kessler et al. 1995). OKWs have been linked to the onset and decay of El Niño (McPhaden and Yu 1999; Zhang and Gottschalck 2002; Seo and Xue 2005). Figure 17 shows a comparison of the OKWs, computed as the bandpass (20–120 days) filtered depth of 20°C isotherm anomalies at 140°W and 1°S–1°N (Seo and Xue 2005), in the CFSR and GODAS with those in the TAO data. Both the CFSR and GODAS agree with

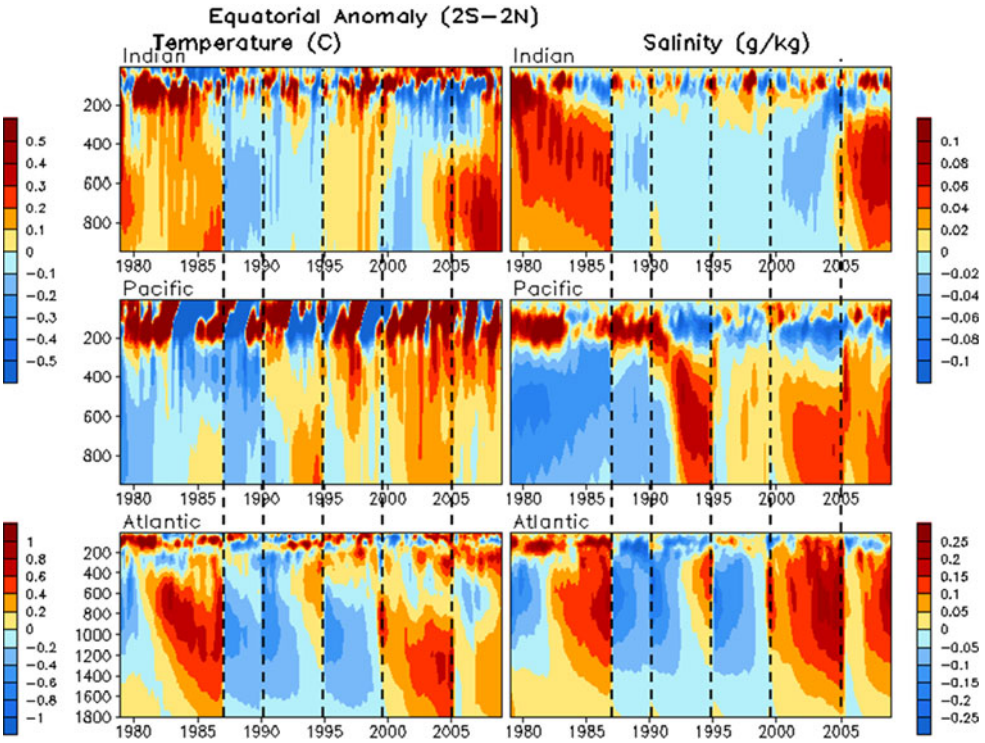

Fig. 15 Depth–time plots of the temperature (*left*, °C) and salinity (*right*, psu) anomaly averaged over the 2°S–N2°N band in the equatorial Indian Ocean (*top row*), the equatorial Pacific Ocean (*middle row*), and the equatorial Atlantic Ocean (*bottom row*). *Vertical dash lines* indicate the beginning of each stream after 1 year spin-up period

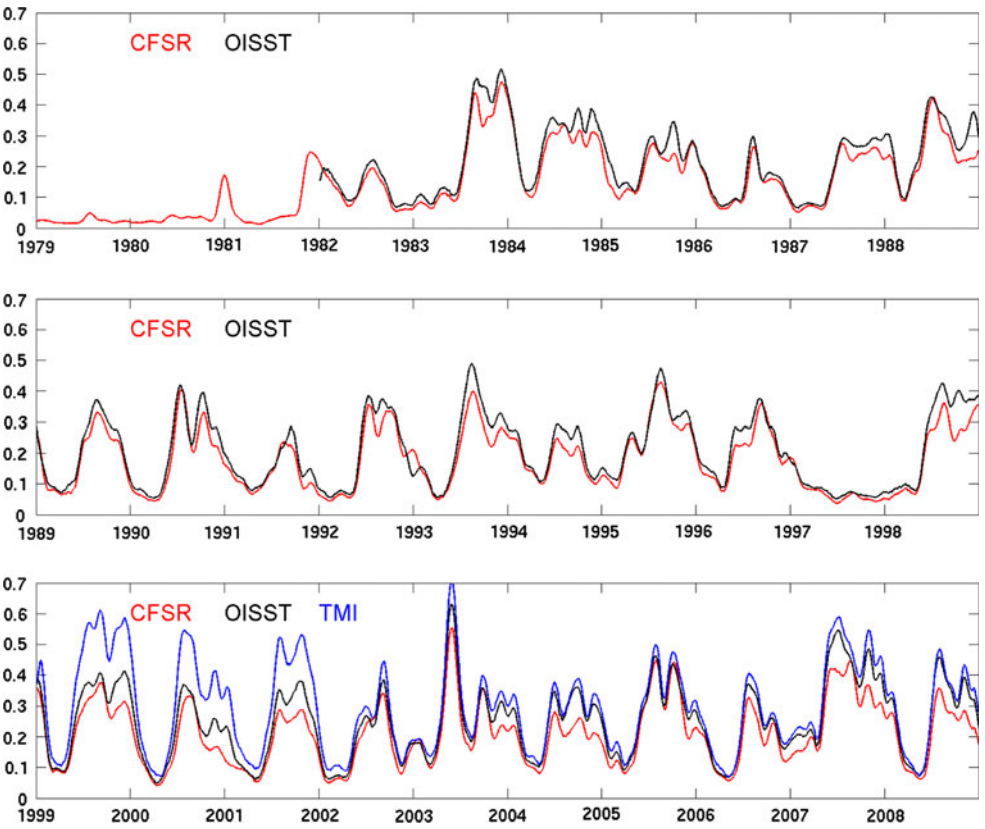

Fig. 16 Time series of the spatial standard deviation in the *box* 160°W–95°W, 0°N–3°N of daily SST anomalies (°C) that are band filtered at periods 20–40 day and wave lengths 890–2,249 km for CFSR (*red line*), OI SST (*black line*) and TMI SST (*blue*). The daily time series has been smoothed by a 30-day running mean

the TAO during 1993–2008, and are also consistent with each other during 1988–1993. However, large discrepancies occur occasionally during 1979–1987. The uncertainties in OKWs in the early period should be considered when the CFSR is used to study the long-term variations of OKWs.

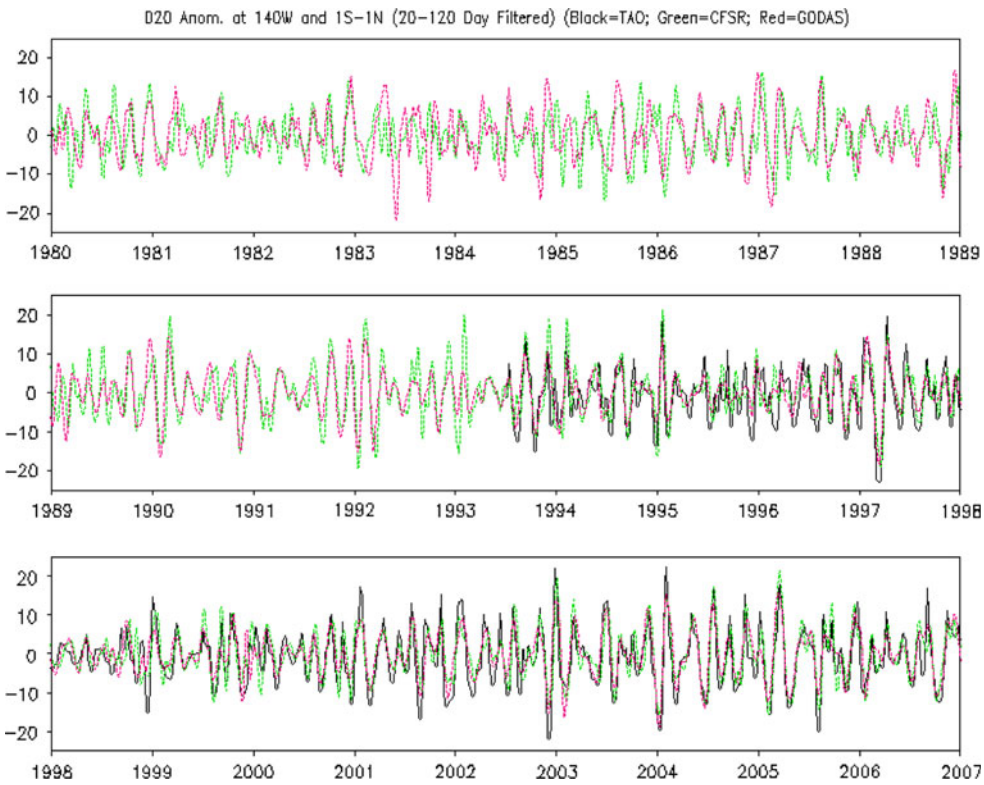

Fig. 17 Depth of the 20°C isotherm anomaly (meter) band filtered at periods 20–120 day at 140°W and averaged over 1°S–1°N from the TAO temperature (*black solid line*), CFSR (*green dashed line*) and GODAS (*red dashed line*)

5.1.3 ENSO

ENSO is the strongest interannual signal in the tropics, and has a significant impact on the global climate. The role of ocean heat content as a precursor for ENSO has been extensively documented in the literature (Wyrtki 1985; Jin 1997). Xue et al. (2000) suggested that there are at least three independent EOF modes of ocean heat content that contribute to ENSO forecast skill. Here we verify if the three EOF modes of HC300a in the CFSR and GODAS are consistent with each other.

Figure 18 shows that the first three EOFs and PCs of HC300a from the CFSR are similar to those from the GODAS, and the associated surface wind stress anomalies are also remarkably similar. The percent variance explained by the three EOFs is also similar, indicating that they are indeed robust EOF modes well captured by both ocean analyses. It should be noted that the means of the CFSR HC300a in 1979–1998 and 1999–2008 have been removed before the EOF calculation. This is because that the CFSR temperature has a persistent warm bias in the eastern Pacific after 1999 (Fig. 11).

5.2 Tropical Indian Ocean

Recently, the IOD has been identified as a coupled ocean–atmosphere interaction phenomenon that features an east–west dipole in SST coupled with surface winds in the tropical Indian Ocean (e.g. Saji et al. 1999). The IOD has a significant influence on global climate such as the Indian summer monsoon, the Australia winter climate, and African rainfall and is also connected with the tropical Pacific ENSO (Yamagata et al. 2004). The first EOF of SST is a basin-wide warming pattern reflecting the forcing of ENSO, and the second EOF is the dipole SST (Yamagata et al. 2004). In contrast, the first EOF of SSHa is a dipole pattern mostly forced by surface winds associated with the IOD (Rao et al. 2002). Off equatorial thermocline variations induced by Rossby wave processes, manifested in the second EOF of SSHa, allow for a possible delayed and negative feedback for the IOD (Rao et al. 2002).

We choose to use the Altimetry SSH to describe the thermocline variations in the tropical Indian Ocean since large uncertainties exist in HC300 due to sparse observations. The first two EOFs and PCs of SSH from the CFSR and Altimetry are shown in Fig. 19. The linear trends in each data have been removed before the EOF calculation because of the large SSH trend in the tropical Indian Ocean (Fig. 8). The EOF1 pattern of SSHa and the corresponding regression pattern of surface wind stress capture the major features of the dipole mode of thermocline variations with a minimum near Java/Sumatra and a maximum in the south-central Indian Ocean around 10°S, and an anti-cyclonic wind anomaly in the southeastern Indian Ocean. The EOF1 and PC1 of the CFSR and GODAS, accounting for 27 and 26% of the total variance, respectively, agree

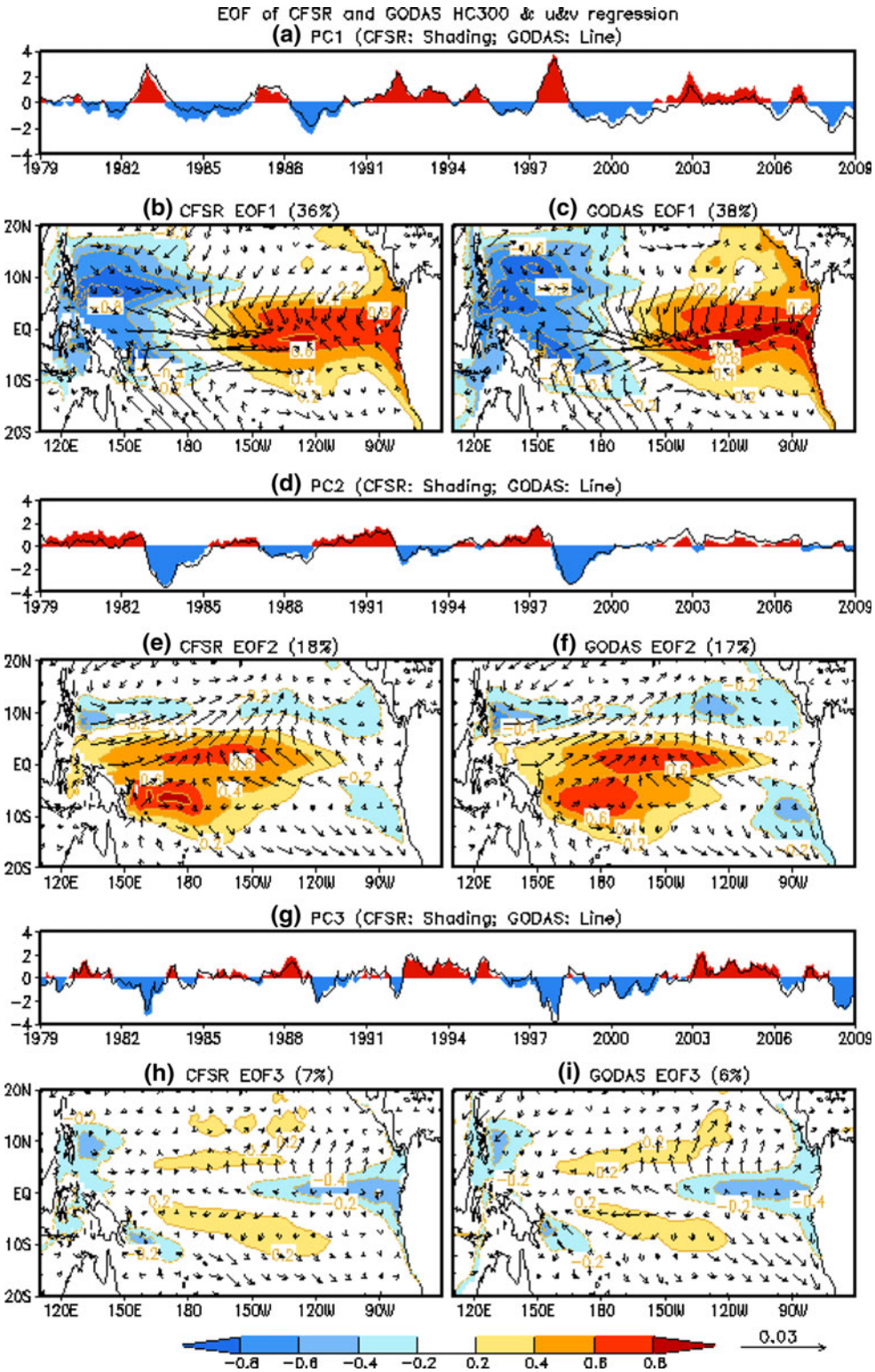

Fig. 18 First three EOFs and PCs of HC300 anomalies (HC300a) (°C) from CFSR (*left panels*) and GODAS (*right panels*) calculated for the period 1979–2008 in the tropical Pacific. Anomalies are based on the 1979–2008 average, and for CFSR the mean anomalies for the periods 1979–1998 and 1999–2008 are further removed to account for the sudden onset of warm bias around 1998/1999 (see Fig. 11). For the time series, *shading* (*line*) represents the CFSR (GODAS). The regression vectors of the wind stress anomalies of CFSR (R2) onto the PCs of CFSR (GODAS) HC300a are overlaid on the EOF patterns

very well with those of the Altimetry, showing the largest amplitude of the positive IOD events in 1982, 1994, 1997 and 2006. The EOF2 mode is similar to the second mode discussed by Rao et al. (2002), who refer to it as a quasi-biennial mode. It is encouraging that the EOF2 and PC2 of the CFSR and GODAS, accounting for 10 and 9% of the total variance, respectively, also agree very well with those of the Altimetry, implying the robustness of this mode. However, some differences in the PC2 of the CFSR and GODAS are noticed prior to 1986, indicating uncertainties in the early period.

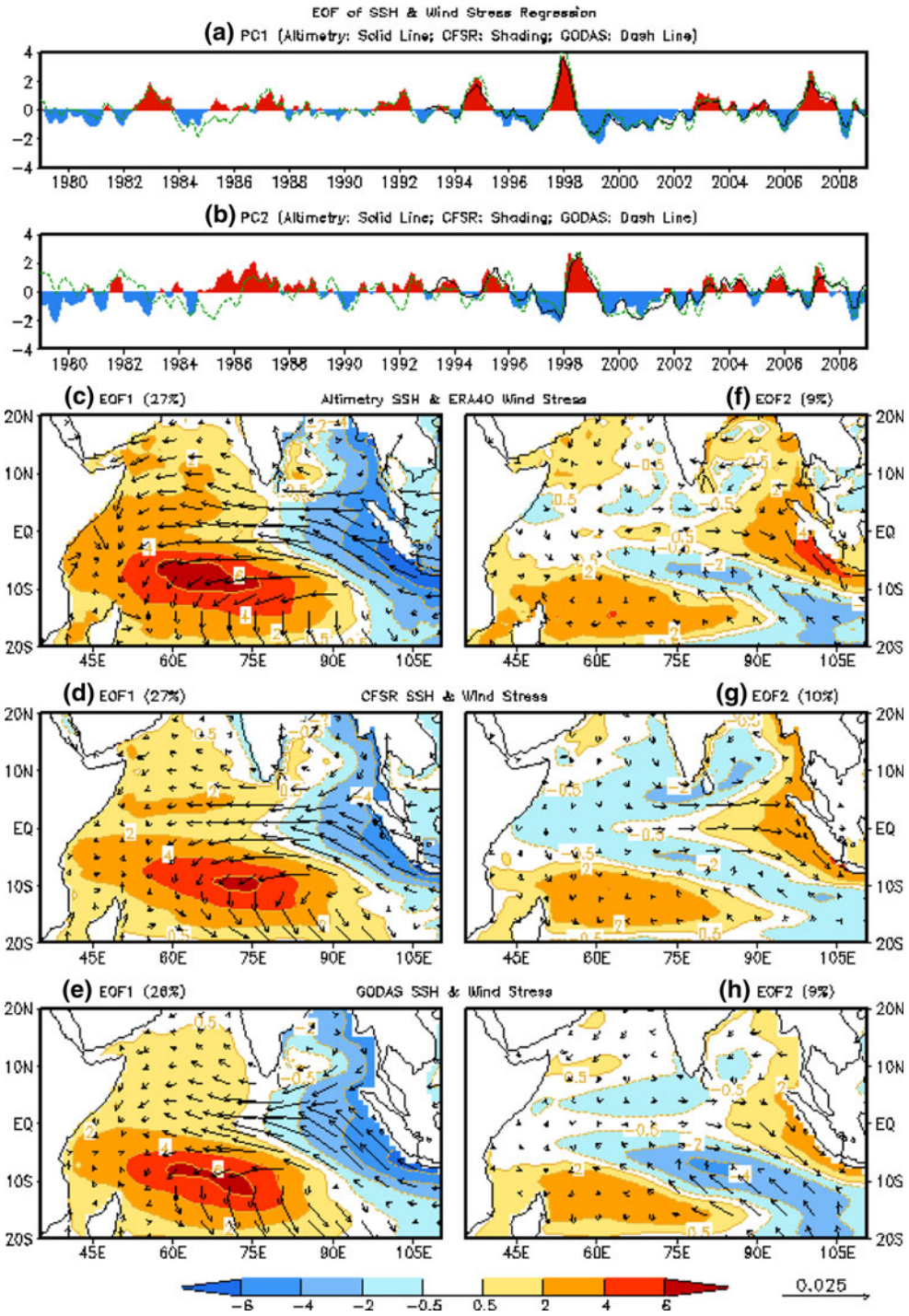

Fig. 19 The first two EOF patterns of the sea surface height anomalies (SSHa) (cm) for **c**, **f** AVISO altimetry for 1993–2008, **d**, **g** CFSR for 1979–2008 and **e**, **h** GODAS for 1979–2008 in the tropical Indian Ocean. The anomalies are relative to an average of the whole period, and a linear trend has been removed prior to the EOF calculation. For **a** the PC1 and **b** the PC2 time series, the *solid* (*dash*) *line* is for the AVISO altimetry (the GODAS), and the *shading* is for the CFSR. The regression vectors of the wind stress anomalies of ERA40 (CFSR, GODAS) onto the PCs of AVISO altimetry (CFSR, GODAS) SSHa are overlaid on the EOF patterns

5.3 North Pacific

Low-frequency fluctuations in the North Pacific are characterized by two dominant modes of oceanic variability, the PDO (Mantua et al. 1997) and the more recently recognized North Pacific Gyre Oscillation (NPGO) (Di Lorenzo et al. 2008, referred to as D08 hereafter). The PDO is defined as the dominant mode of variability of North Pacific SSTa, which is highly correlated with the dominant mode of SSHa (Chhak et al. 2009, referred to as C09). The NPGO is defined as the second dominant mode of SSHa in the Northeast Pacific, and is highly correlated with the second mode of North Pacific SSTa, also referred to as the Victoria Mode (Bond et al. 2003). Since the NPGO significantly correlates with decadal variations of salinity, nutrients and coastal upwelling, it is also a good indicator of decadal changes in marine ecosystems (D08).

The temperature and salinity signature of the PDO and the NPGO is largely confined in the top 300 m of the water column (C09). Therefore, we use HC300a to describe the PDO and NPGO modes. The first two EOF patterns of HC300a from NODC, CFSR and GODAS in 1979–2008 and their corresponding PC time series are shown in Fig. 20. The EOF1 of the NODC (Fig. 20c) resembles the EOF1 of SSH (D08), characterized by negative anomalies in the central northeast Pacific flanked by positive anomalies along the west coast of North America, and in the Gulf of Alaska and Bering Sea. The regression pattern of surface wind stress anomalies onto the PC1 (vector in Fig. 20c) resembles an enhanced Aleutian Low—the first mode of sea level pressure (SLP) anomaly in the North Pacific (Trenberth and Hurrell 1994). The EOF1 of the CFSR and GODAS generally agrees with that of the

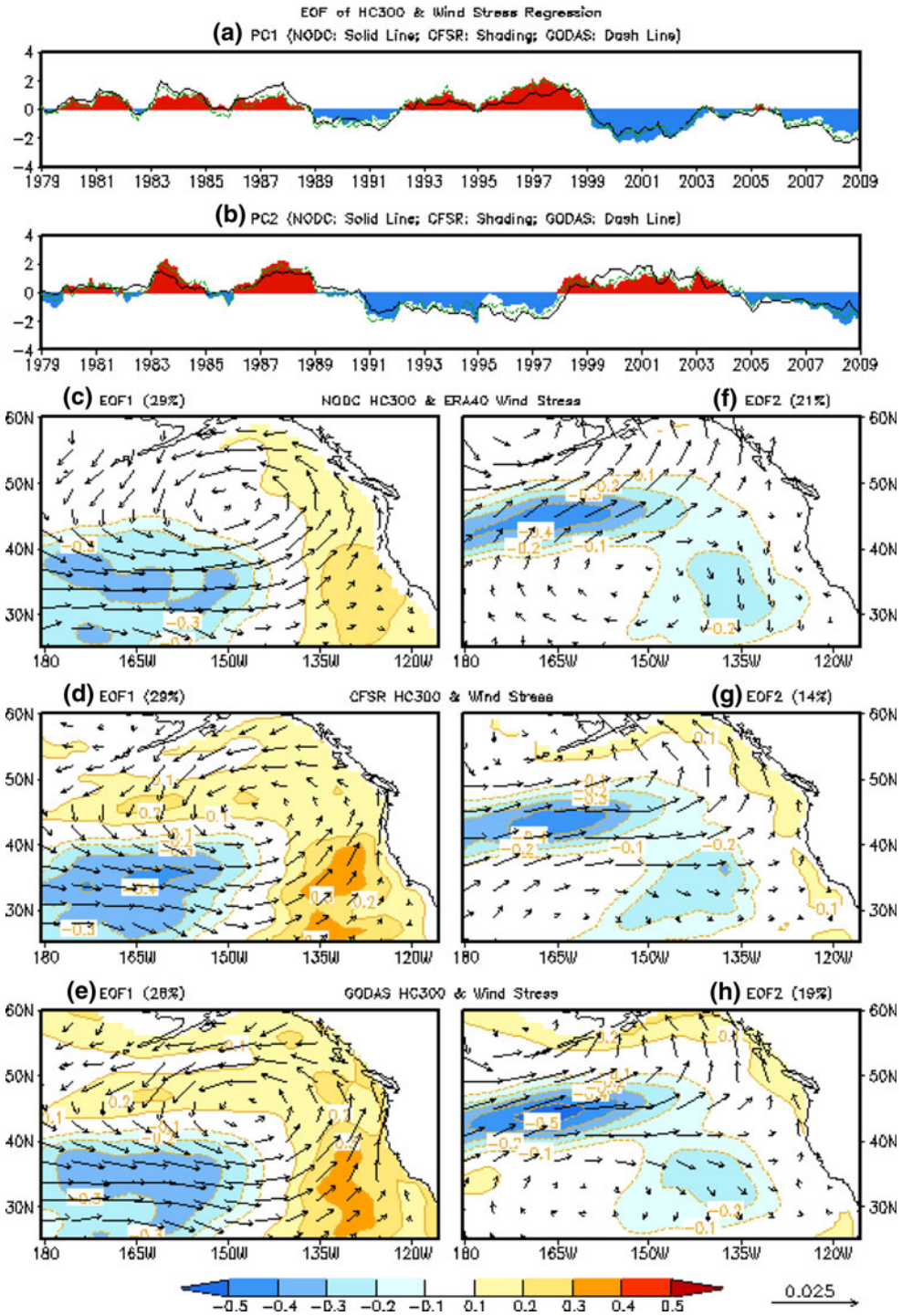

Fig. 20 The first two EOF patterns of HC300 anomalies (HC300a) (°C) for **c**, **f** NODC, **d**, **g** the CFSR and **e**, **h** GODAS for the period 1979–2008 in the North Pacific. Anomalies are relative to the average for the period 1979–2008. For the **a** PC1 and **b** PC2 time series, the *solid* (*dash*) *line* represents the NODC (GODAS), and the *shading* is the CFSR. The regression vectors of wind stress anomalies of ERA40 (CFSR, GODAS) onto the PCs of the NODC (CFSR, GODAS) SSHa are overlaid on the EOF patterns

NODC except the positive anomalies in the high-latitude North Pacific are too strong and extend too far south. The PC1 of the CFSR and GODAS agrees very well with the PC1 of the NODC (Fig. 20a). The EOF1 accounts for 29, 29 and 28% of the total variance for NODC, CFSR and GODAS, respectively.

The EOF2 of the NODC is characterized by a zonal band of negative anomalies between 40°N and 50°N extending southeastward in the subtropical northeast Pacific (Fig. 20f). The associated surface wind stress anomalies indicate positive (negative) SLPa in the subtropical (subpolar) North Pacific, which is associated with the second mode of North Pacific SLP (Walker and Bliss 1932). The EOF2 accounts for 21, 14 and 19% of the total variance for NODC, CFSR and GODAS, respectively. The EOF2 and PC2 of the CFSR and GODAS generally agree with those of the NODC.

It is worthwhile to point out that the EOF2 of SSHa has a dipole pattern with negative (positive) anomalies located to the north (south) of 40°N (D08). It is shown in C09 that negative (positive) salinity anomalies are collocated with positive (negative) temperature anomalies and their contributions to SSHa are additive, therefore enhancing SSHa variability. However, the positive temperature anomalies south of 40°N are much weaker than the negative temperature anomalies north of 40°N (C09). Therefore, the dipole SSHa pattern corresponds to the one pole HC300a pattern (Fig. 20f–h).

5.4 North Atlantic

The EOF1 of the altimetry SSHa shows a weakening of the North Atlantic subpolar gyre since 1995 (Hakkinen and Rhines 2004), which is thought to be an indicator of a slowdown of the AMOC. Boning et al. (2006) suggest that the recent slowing subpolar gyre reflects a slowdown of the deep western boundary current off Labrador, with consequences on the strength of the AMOC in the subtropical North Atlantic. These studies suggest that the PC1 of SSHa or UOHCa is an indicator of the strength of the subpolar gyre, and perhaps, can be regarded as the fingerprint of the AMOC (Zhang 2008) (Fig. 21).

The EOF analysis of the NODC annual mean HC300a in 1956-2008 reveals two significant modes that account for 53 and 12% of the total variance, respectively. The EOF1 and PC1 represent a warming trend of HC300a since 1993, and the warming covers the entire North Atlantic with the largest amplitude in the Labrador and Irminger Sea. The projection of the Altimetry onto the EOF1 of the NODC agrees well with the PC1 of the NODC, suggesting that the PC1 is robust. The EOF1 and PC1 of the CFSR are similar to those of the NODC except that the warming in the Labrador Sea is underestimated. The regression of CFSR wind stress onto the PC1 of the CFSR shows easterly wind anomalies over the maximum warming region.

The EOF2 of the NODC is similar to the EOF1 of the altimetry SSHa discussed by Hakkinen and Rhines (2004) and Zhang (2008). The EOF2 and PC2 of the CFSR agree well with those of the NODC except the CFSR shows an initial spin up during the first 4-year integration. The PC2 indicates that the subpolar gyre trended upward from the mid-60s, reaching a maximum in 1995, followed by a rapid decline in 1996–1997, a rapid strengthening from 1998 to 2000, followed by a downward trend from 2000 to 2008. The time evolution of the EOF2 is largely driven by changes in heat flux and wind stress associated with the North Atlantic Oscillation (NAO) (Boning et al. 2006). In fact, the regression pattern of CFSR wind stress shows a cyclonic (anti-cyclonic) circulation to the north (south) of 45°N, consistent with a positive NAO phase.

The CFSR is superior to the GODAS in simulation of the two dominant modes. For example, the EOF1 of the GODAS underestimates the maximum in the Labrador Sea, and overestimates the minimum near 58°W and 44°N. The PC1 and PC2 of the GODAS also have too much high frequency variability. The possible reasons for the improvement in HC300 simulation in the CFSR include an interactive sea ice, better net surface heat fluxes (Fig. 1) and better wind stress in North Atlantic (Figs. 3, 4).

6 Summary and conclusions

Recently, a new high resolution reanalysis from 1979–2009, the CFSR, was completed at the NCEP (Saha et al. 2010). The CFSR uses a partially coupled ocean and atmosphere data assimilation system. The oceanic component of the CFSR, representing a new global ocean analysis, will replace the current operational ocean analysis produced by the Global Ocean Data Assimilation System (GODAS). Compared to the GODAS, the oceanic component of the CFSR includes many advances: (a) the MOM4 ocean model with an interactive sea-ice, (b) a 6 h coupled model forecast as the first guess field, (c) inclusion of the mean climatological river runoff, and (d) high spatial (0.5° × 0.5°) and temporal (hourly) model output. The analysis presented in this paper is meant to inform the user community about the salient features in the CFSR ocean component, and how the ocean reanalysis compares with in situ observations and previous reanalysis.

The main features on the climatology and interannual variability of surface heat and momentum fluxes and various oceanic fields are summarized below:

- The net ocean surface heat flux of the CFSR has smaller biases compared to the combination of the LH and SH

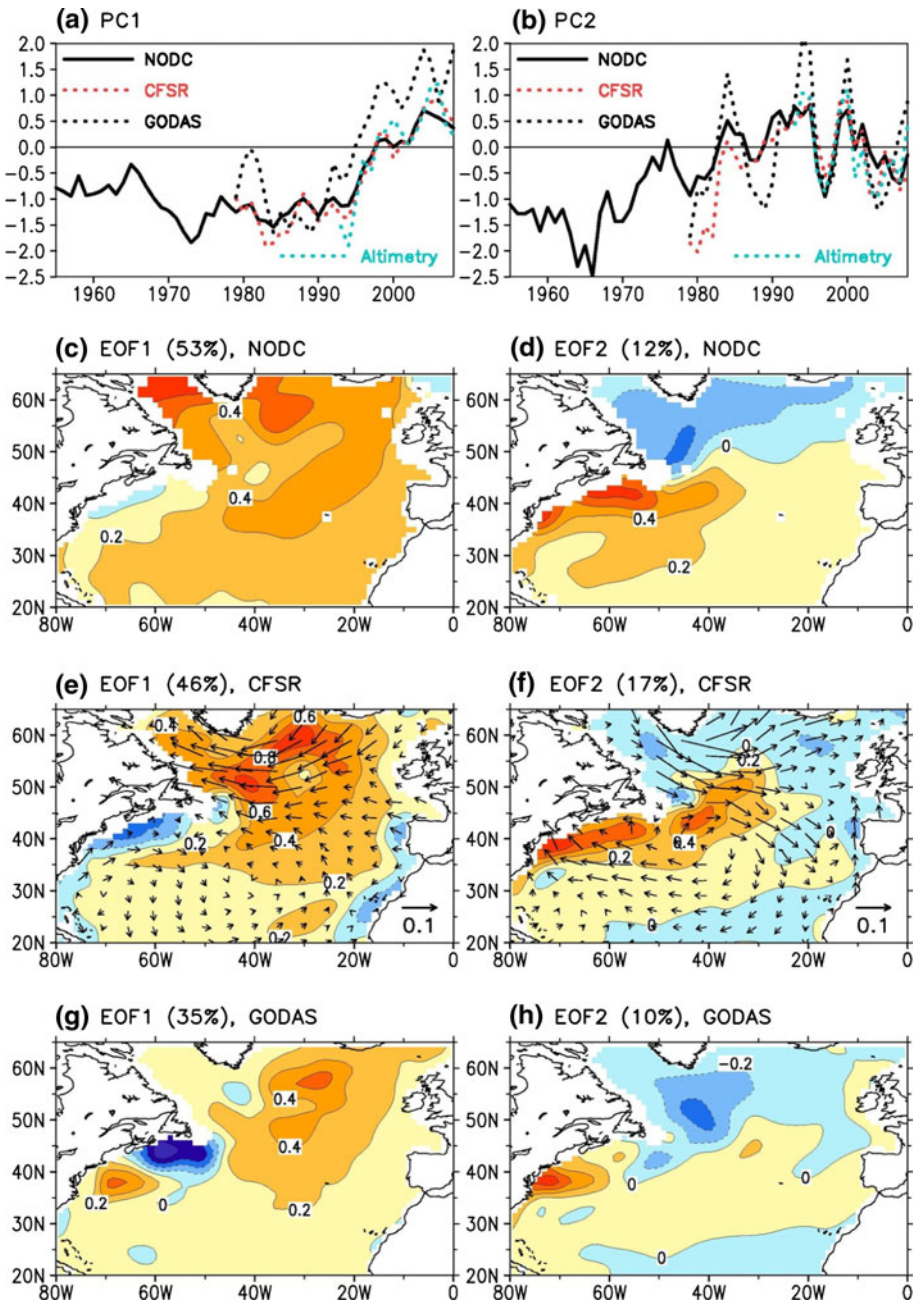

Fig. 21 The first two EOFs and PCs of the HC300 anomalies (HC300a) (°C) for **c**, **d** NODC for the period 1956–2008, **e**, **f** the CFSR and **g**, **h** the GODAS for the period 1979–2008 in the North Atlantic. The anomalies are relative to the 1993–2008 average. For the **a** PC1 and **b** PC2 time series, the NODC is represented by the *black solid line*, the CFSR by the *red dotted line* and the GODAS by the *black dotted line*. Also included are the regression coefficients of the AVISO altimetry onto the EOFs (*blue dotted line*). The regression vectors of the CFSR wind stress anomalies (dyn/cm^2) onto the PCs of CFSR HC300a are overlaid on the EOF patterns of CFSR HC300a

from the OAFlux and the SW and LW from the ISCCP than the R1 and R2 in both the tropics and extratropics. However, an imbalance in the mean net heat flux over the global oceans is larger (14.7 W/m^2) in the CFSR than that in R1 (4.5 W/m^2) and R2 (4.7 W/m^2). There is a sudden increase (decrease) of net heat flux (latent heat flux) around 1998/1999 with the assimilation of the ATOVS radiance data starting in October 1998.

- The ocean surface wind stress of the CFSR has smaller biases and higher correlation with the ERA40 than the R1 and R2, particularly in the tropical Indian and Pacific Ocean. The CFSR wind stress climatology also compares with the QuickSCAT climatology better than the R1 and R2 for the period September 1999–October 2009. However, the trade winds in the central tropical Pacific are too strong prior to 1999, and become close to the observations once the ATOVS radiance data are assimilated in October 1998. A sudden reduction of easterly wind bias is related to the sudden onset of a warm bias in the equatorial eastern Pacific temperature around 1998/1999.
- In the equatorial Pacific, compared with the TAO temperature, TAO currents and OSCAR currents, the CFSR generally has lower skill than the GODAS,

because of the changes in the means in the period 1979-1998 and 1999-2008 associated with the onset of a warm bias in the equatorial Pacific temperature around 1998/1999.

- The CFSR SST is about 0.2–0.4°C colder than the weekly OI SST except near the western boundary currents. The anomaly correlation is above 0.8 over most of the global ocean, except near the western boundary currents, in the Bay of Bengal and mid- and high-latitude southern oceans. The RMSDs are mostly less than 0.3°C except over the western boundary currents. In summary, the CFSR SST agrees with the OI SST much better than the GODAS SST.
- An error (discovered late during the execution of the CFSR) damped SSS variability on both seasonal and interannual time scales.
- As compared to the NODC, the linear trend of HC300 in 1993–2008 is simulated better by the CFSR than by the GODAS in the mid- and high-latitude oceans, but worse in the equatorial eastern Pacific and the tropical Atlantic.
- As compared to the altimetry, SSH variability is simulated better by the CFSR than by the GODAS in the tropical Indian Ocean and extratropics, but worse in the tropical Atlantic, which is related to the drifts in the deep ocean.
- Drifts in the subsurface temperature and salinity within each data stream are relatively small in the equatorial Pacific and Indian Ocean, but are quite large in the equatorial Atlantic.
- Initial spin up has adverse impacts on the first stream, and changes of observations may cause abrupt changes in the subsurface temperature and salinity.

In summary, the surface heat fluxes and wind stress from the CFSR generally agree with observations better than the R1 and R2. A complementary assessment of the fresh water fluxes by Wang et al. 2010 suggests the fresh water fluxes (precipitation minus evaporation) from the CFSR also agree with observations better. The CFSR SST is significantly better than the GODAS SST, and the HC300 and SSH are also improved in the tropical Indian Ocean and extratropics. A few deficiencies are noticed. Firstly, the trade winds in the central tropical Pacific are too strong prior to 1999, and become close to observations once the ATOVS radiance data are assimilated in October 1998. A sudden reduction of easterly wind bias is related to the sudden onset of a warm bias in the equatorial eastern Pacific temperature around 1998/1999, which has implications for ENSO prediction. Secondly, the use of six data streams in the CFSR leads to large discontinuity in the deep ocean temperature and salinity, which contributes to the degradation of the SSH kill in the tropical Atlantic. Thirdly, a too strong nudging to the annual mean SSS damped SSS variability completely. To correct the above deficiencies, a stand-alone GODAS, which assimilates the same in situ data, but forced by the CFSR surface fluxes, will be developed and evaluated. If it is found to be superior to the CFSR, it will be used for the global ocean monitoring products (http://www.cpc.ncep.noaa.gov/products/GODAS).

The main features on simulation of Tropical Instability Waves (TIW) and oceanic Kelvin waves in the tropical Pacific, and the dominant modes of HC300 that are associated with ENSO, IOD, Pacific Decadal Oscillation (PDO) and Atlantic Meridional Overturning Circulation (AMOC) are summarized below:

- SST anomalies associated with Tropical Instability Wave (TIW) in the CFSR are similar to those in the daily OI SST and TMI SST.
- Thermocline variations in the equatorial Pacific at periods of 20-120 days are used to represent oceanic Kelvin waves (OKWs). The OKWs in the CFSR are consistent with those in the TAO and GODAS. However, disagreements between the CFSR and GODAS are apparent prior to 1987.
- There are at least three independent EOF modes of HC300 that contribute to ENSO forecast skill (Xue et al. 2000). The first three EOFs and PCs of HC300a from the CFSR are similar to those from the GODAS once the 1979–1998 and 1999–2008 means in the CFSR are removed prior to EOF calculation to account for the sudden onset of a warm bias after 1999.
- The first two EOFs and PCs of SSHa in the tropical Indian Ocean in the CFSR and GODAS are similar to those in the altimetry. Some disagreements between the PC2 of the CFSR and GODAS are apparent prior to 1986, indicating uncertainties in the early period. The EOF1 represents the IOD, and the EOF2 is related to the quasi-biennial oscillation (Rao et al. 2002).
- The first two EOFs and PCs of HC300a in the Northeast Pacific in the CFSR and GODAS are consistent with those in the NODC. The EOF1 represents the PDO, and the EOF2 is the recently identified North Pacific Gyre Oscillation (NPGO) (Di Lorenzo et al. 2008; Chhak et al. 2009), which significantly correlates with decadal variations of salinity, nutrients and coastal upwelling.
- The first two EOFs and PCs of HC300a in the North Atlantic in the CFSR are similar to those in the NODC, while those of the GODAS have some biases. The improvements in HC300 simulation in the CFSR are probably attributable to an interactive sea ice and better surface heat and momentum fluxes in North Atlantic. The EOF1 represents the warming trend since 1990 and the EOF2 features a strengthening of the subpolar gyre

and subtropical gyre, which can be regarded as the fingerprint of the AMOC (Zhang 2008).

Acknowledgments The authors thank Mike Halpert and Wanqiu Wang, and the two anonymous reviewers for their thorough reviews of the manuscript. We are also thankful for (1) the altimeter products produced by Ssalto/Duacs and distributed by Aviso with support from CNES, (2) the seasonal mean temperature and 5-year mean salinity analysis and the World Ocean Atlas by National Oceanographic Data Center, (3) the TAO mooring data by NOAA, (4) the Objectively Analyzed air-sea Fluxes (OAFlux) by Woods Hole Oceanographic Institution, (5) the ISCCP global radiative flux by NASA Goddard Institute for Space Studies, (6) the Ocean Surface Current Analysis-Real Time (OSCAR) by Earth and Space Research, (7) the TRMM Microwave Imager (TMI) SST by Remote Sensing Systems.

References

Antonov JI, Locarnini RA, Boyer TP, Mishonov AV, Garcia HE (2006) World Ocean Atlas 2005, vol 2, Salinity. Levitus S. (ed) NOAA Atlas NESDIS 62, US Government Printing Office, Washington, DC, 182 pp

Argo Science Team (2001) The global array of profiling floats. In: Koblinsky CJ, Smith NR (eds) Observing the ocean in the 21st century. Australian Bureau of Meteorology, London, pp 248–258

Balmaseda M, Anderson D (2009) Impact of initialization strategies and observations on seasonal forecast skill. Geophys Res Lett 36:L01701. doi:10.1029/2008GL035561

Balmaseda MA, Vidard A, Anderson D (2008) The ECMWF ORA-S3 ocean analysis system. Mon Weather Rev 136:3018–3034

Balmaseda M et al (2010) Role of the ocean observing system in an end-to-end seasonal forecasting system. In: Hall J, Harrison DE, Stammer D, (eds) Proceedings of oceanobs'09: sustained ocean observations and information for society (vol 2), Venice, Italy, 21–25 September 2009. ESA Publication WPP-306, Venice

Behringer DW (2007) The global ocean data assimilation system at NCEP. In: 11th Symposium on integrated observing and assimilation systems for atmosphere, oceans, and land surface, AMS 87th annual meeting, San Antonio, Texas, 12 pp

Behringer DW, Xue Y (2004) Evaluation of the global ocean data assimilation system at NCEP. In: The Pacific Ocean. Eighth symposium on integrated observing and assimilation system for atmosphere, ocean, and land surface, AMS 84th annual meeting, Washington State Convention and Trade Center, Seattle, Washington, DC, pp 11–15

Behringer DW, Ji M, Leetmaa A (1998) An improved coupled model for ENSO prediction and implications for ocean initialization. Part I. The ocean data assimilation system. Mon Weather Rev 126:1013–1021

Berry DI, Kent EC (2009) A new air-sea interaction gridded dataset from ICOADS with uncertainty estimates. Bull Am Met Soc 90:645–656

Bond NA, Overland JE, Spillane M, Stabeno P (2003) Recent shifts in the state of the North Pacific. Geophys Res Lett 30(23):2183. doi:10.1029/2003GL018597

Boning CW, Scheinert M, Dengg J, Biastoch A, Funk A (2006) Decadal variability of subpolar gyre transport and its reverberation in the North Atlantic overturning. Geophys Res Lett 33:L21S01. doi:10.1029/2006GL026906

Bonjean F, Lagerloef GSE (2002) Diagnostic model and analysis of the surface currents in the tropical pacific ocean. J Phys Oceanogr 32:2938–2954

Bourlès B, Lumpkin R, McPhaden MJ, Hernandez F, Nobre P, Campos E, Yu L, Planton S, Busalacchi AJ, Moura AD, Servain J, Trotte J (2008) The PIRATA program: history, accomplishments, and future directions. Bull Am Met Soc 89:1111–1125

Carton JA, Santorelli A (2008) Global upper ocean heat content as viewed in nine analyses. J Clim 21:6015–6035

Chelliah M, Ebisuzaki W, Weaver S, Kumar A (2010) Evaluating the tropospheric analyses from NCEP's climate forecast system reanalysis. Clim Dyn (submitted)

Chhak KC et al (2009) Forcing of low-frequency ocean variability in the northeast Pacific. J Clim 22:1255–1276

Conkright ME et al (1999) World ocean database 1998, documentation and quality control version 2.0. National oceanographic data center internal report 14. National Oceanographic Data Center, Silver Spring

de Boyer Montegut C, Mignot J, Lazar A, Cravatte S (2007) Control of salinity on the mixed layer depth in the world ocean. 1. General description. J Geophys Res 112:C06011. doi:10.1029/2006JC003953

Derber J, Rosati A (1989) A global oceanic data assimilation system. J Phys Oceanogr 19:1333–1347

Di Lorenzo E et al (2008) North Pacific Gyre Oscillation links ocean climate and ecosystem change. Geophys Res Lett 35:L08607. doi:10.1029/2007GL032838

Duing W et al (1975) Meanders and long waves in the equatorial Atlantic. Nature 257:280–284

Griffies SM, Harrison MJ, Pacanowski RC, Rosati A (2004) Technical guide to MOM4, GFDL ocean group technical report no. 5. NOAA/Geophysical Fluid Dynamics Laboratory. Available on-line at http://www.gfdl.noaa.gov/~fms

Guilyardi E, Wittenberg A, Fedorov A, Collins M, Wang C, Capotondi A, van Oldenborgh GJ, Stockdale T (2009) Understanding El Nino in ocean-atmosphere general circulation models. Bull Am Met Soc 90:325–340

Hakkinen S, Rhines PB (2004) Decline of subpolar North Atlantic circulation during the 1990s. Science 304:555–559

Hashizume H, Takeuchi K, Xie SP, Liu WT (2001) Local and remote atmospheric response to tropical instability waves- A global view from space. J Geophys Res 106:10173–10185

Hu ZZ, Huang B, Pegion K (2008) Low-cloud errors over the southeastern Atlantic in the NCEP CFS and their association with lower-tropospheric stability and air-sea interaction. J Geophys Res 113:D12114. doi:10.1029/2007JD009514

Huang B, Xue Y, Behringer DW (2008) Impacts of argo salinity in NCEP global ocean data assimilation system: the tropical Indian Ocean. J Geophys Res 113:C08002. doi:10.1029/2007JC004388

Ji M, Leetmaa A, Derber J (1995) An ocean analysis system for seasonal to interannual climate studies. Mon Wea Rev 123:460–481

Jin FF (1997) An equatorial ocean recharge paradigm for ENSO. Part I. Conceptual model. J Atmos Sci 54:811–829

Jochum M, Murtugudde R (2006) Temperature advection by tropical instability waves. J Phys Oceanogr 36:592–605

Josey SA, Kent EC, Taylor PK (2002) Wind stress forcing of the ocean in the SOC climatology: Comparisons with the NCEP–NCAR, ECMWF, UWM/COADS, and Hellerman and Rosenstein Datasets. J Phys Oceanogr 32:1993–2019

Kalnay E et al (1996) The NCEP/NCAR 40-Year Reanalysis Project. Bull Am Met Soc 77:437–471

Kanamitsu M, Ebitsuzaki W, Woolen J, Yang SK, Hnilo JJ, Fiorino M, Potter GL (2002) NCEP-DOE AMIP-II reanalysis (R-2). Bull Am Met Soc 83:1631–1643

Keppenne CL, Rienecker MM, Jacob JP, Kovach R (2008) Error covariance modeling in the GMAO ocean ensemble kalman filter. Mon Wea Rev 136:2964–2982

Kessler WS, McPhaden MJ, Weickmann KM (1995) Forcing of intraseasonal Kelvin waves in the equatorial Pacific. J Geophys Res 100:10613–10631

Kohl A, Stammer D (2008) Decadal sea level changes in the 50-year GECCO ocean synthesis. J Clim 21:1876–1890
Large WG, Yeager SG (2009) The global climatology of an interannually varying air-sea flux data set. Clim Dyn 33:341–364
Levitus S (1986) Annual cycle of salinity and salt storage in the World Ocean. J Phys Oceanogr 16:322–343
Levitus S, Antonov JI, Boyer TP, Locarnini RA, Garcia HE, Mishonov AV (2009) Global ocean heat content 1955–2008 in light of recently revealed instrumentation problems. Geophys Res Lett 36:L07608. doi:10.1029/2008GL037155
Locarnini RA, Mishonov AV, Antonov JI, Boyer TP, Garcia HE (2006) World Ocean Atlas 2005, volume 1. Temperature. In: Levitus S (ed) NOAA Atlas NESDIS 61, US Government Printing Office, Washington, DC, 182 pp
Long CS, Butler AH, Lin R, Wild J, Yang SK, Zhou S, Liu H (2010) Evaluation of the stratosphere in the NCEP climate forecast system reanalysis. Clim Dyn (submitted)
Lukas R, Lindstrom E (1991) The mixed layer of the western equatorial Pacific Ocean. J Geophys Res 96:3343–3357
Mantua NJ, Hare SJ, Zhang Y, Wallace JM, Francis RC (1997) A Pacific interdecadal oscillation with impacts on salmon production. Bull Amer Met Soc 78:1069–1079
McPhaden MJ, Yu X (1999) Equatorial waves and the 1997–98 El Niño. Geophys Res Lett 26:2961–2964
McPhaden MJ et al (1998) The tropical ocean–global atmosphere (TOGA) observing system: a decade of progress. J Geophys Res 103:14,169–14,240
McPhaden MJ et al (2009) RAMA: the research moored array for African–Asian–Australian monsoon analysis and prediction. Bull Amer Met Soc 90:459–480
Meehl GA et al (2009) Decadal prediction: can it be skillful? Bull Am Met Soc 90:1467–1485
Qiao L, Weisberg RH (1995) Tropical instability wave kinematics: observations from the tropical instability wave experiment. J Geophys Res 100:8677–8694
Rao SA, Behera SK, Masumoto Y, Yamagata T (2002) Interannual subsurface variability in the tropical Indian Ocean with a special emphasis on the Indian Ocean dipole. Deep Sea Res II 49:1549–1572
Rayner NA et al (2003) Global analyses of sea surface temperature, sea ice, and night marine air temperature since the late nineteenth century. J Geophys Res 108(D14):4407. doi:10.1029/2002JD002670
Renfrew IA, Moore GWK, Guest PS, Bumke K (2002) A comparison of surface layer and surface turbulent-flux observations over the Labrador Sea with ECMWF analyses and NCEP reanalyses. J Phys Oceanogr 32:383–400
Reynolds RW, Rayner NA, Smith TM, Stokes DC, Wang W (2002) An improved in situ and satellite SST analysis for climate. J Clim 15:1609–1625
Reynolds RW, Smith TM, Liu C, Chelton DB, Casey KS, Schlax MG (2007) Daily high-resolution blended analyses for sea surface temperature. J Clim 20:5473–5496
Risien CM, Chelton DB (2008) A global climatology of surface wind and wind stress fields from eight years of QuikSCAT scatterometer data. J Phys Oceanogr 38:2379–2413
Saha S et al (2010) The NCEP climate forecast system reanalysis. Bull Am Met Soc 91:1015–1057
Saji NH, Goswami BN, Vinayachandran PN, Yamagata T (1999) A dipole mode in the tropical Indian Ocean. Nature 401:360–363
Schneider EK, Huang B, Zhu Z, DeWitt DG, Kinter JL III, Kirtman B, Shukla J (1999) Ocean data assimilation, initialization, and predictions of ENSO with a coupled GCM. Mon Wea Rev 127:1187–1207
Seo KH, Xue Y (2005) MJO-related oceanic Kelvin waves and the ENSO cycle: a study with the NCEP global ocean data assimilation system. Geophys Res Lett 32:L07712. doi:10.1029/2005GL022511
Smith SR, Legler D, Verzone KV (2001) Quantifying uncertainties in NCEP reanalyses using high-quality research vessel observations. J Clim 14:4062–4072
Sprintall J, Tomczak M (1992) Evidence of the barrier layer in the surface layer of the tropics. J Geophys Res 97:7305–7316
Stammer D, Ueyoshi K, Large W, Josey S, Wunsch C (2004) Estimating air–sea fluxes of heat, freshwater and momentum through global ocean data assimilation. J Geophys Res 109. doi:10.1029/2003JC002082
Taylor P (ed) (2000) Final report of the joint WCRP/SCOR Working Group on air–sea fluxes: intercomparison and validation of ocean–atmosphere energy flux fields, WCRP-112, WMO/TDNo. 1036. World Climate Research Programme, 303 pp
Trenberth KE, Hurrell JW (1994) Recent observed interdecadal climate changes in the Northern Hemisphere. Clim Dyn 9:303–319
Trenberth KE, Stepaniak DP, Hurrell JW, Fiorino M (2001) Quality of reanalyses in the tropics. J Clim 14:1499–1510
Uppala SM et al (2005) The ERA-40 re-analysis. Q J R Meteor Soc 131:2961–3012
Walker G, Bliss E (1932) World weather V. Mem Roy Meteor Soc 4:53–84
Wang W, McPhaden MJ (1999) The surface-layer heat balance in the equatorial Pacific Ocean. Part I. Mean seasonal cycle. J Phys Oceanogr 29:1812–1831
Wang W, Xie P, Yoo SH, Xue Y, Kumar A, Wu X (2010) An assessment of the surface climate in the NCEP Climate Forecast System Reanalysis. Clim Dyn (Conditionally accepted)
Willis JK, Roemmich D, Cornuelle B (2004) Interannual variability in upper ocean heat content, temperature, and thermosteric expansion on global scales. J Geophys Res 109:C12036. doi:10.1029/2003JC002260
Wittenberg AT (2004) Extended wind stress analyses for ENSO. J Clim 17:2526–2540
Wyrtki K (1985) Water displacements in the Pacific and the genesis of El Niño cycles. J Geophys Res 90:7129–7132
Xue Y, Leetmaa A, Ji M (2000) ENSO prediction with Markov models: the impact of sea level. J Clim 13:849–871
Xue Y et al (2010) Ocean state estimation for global ocean monitoring: ENSO and beyond ENSO. In: Hall J, Harrison DE, Stammer D (eds) Proceedings of ocean obs'09: sustained ocean observations and information for society (vol 2), Venice, Italy, 21–25 September 2009, ESA Publication WPP-306
Yamagata T, Behera SK, Luo JJ, Masson S, Jury M, Rao SA (2004) Coupled ocean-atmosphere variability in the tropical Indian Ocean. In: Wang C, Xie S-P, Carton JA (eds) Earth climate: the ocean–atmosphere interaction. Geophys Monogr 147, AGU, Washington, DC, pp 189–212
Yu L, Weller RA (2007) Objectively analyzed air-sea heat fluxes (OAFlux) for the global ocean. Bull Am Met Soc 88:527–539
Zeng X, Zhao M, Dickinson RE (1998) Intercomparison of bulk aerodynamical algorithms for the computation of sea surface fluxes using TOGA COARE and TAO data. J Clim 11:2628–2644
Zhang R (2008) Coherent surface-subsurface fingerprint of the Atlantic meridional overturning circulation. Geophys Res Lett 35:L20705. doi:10.1029/2008GL035463
Zhang C, Gottschalck J (2002) SST anomalies of ENSO and the Madden-Julian Oscillation in the equatorial Pacific. J Clim 15:2429–2445
Zhang Y, Rossow W, Lacis A, Oinas V, Mishchenko M (2004) Calculation of radiative flux profiles from the surface to top-of atmosphere based on ISCCP and other global data sets: refinements of the radiative transfer model and input data. J Geophys Res 109. doi:10.1029/2003JD004457
Zhang S, Harrison MJ, Rosati A, Wittenberg A (2007) System design and evaluation of coupled ensemble data assimilation for global oceanic studies. Mon Wea Rev 135:3541–3564